8-2015

Development, optimization, and implementation of a vibration based defect detection algorithm for railroad bearings

Amy Gonzalez
University of Texas-Pan American

DEVELOPMENT, OPTIMIZATION, AND IMPLEMENTATION OF A VIBRATION BASED DEFECT DETECTION ALGORITHM FOR RAILROAD BEARINGS

A Thesis

by

AMY GONZALEZ

Submitted to the Graduate School of
The University of Texas-Pan American
In partial fulfillment of the requirements for the degree of

MASTER OF SCIENCE

August 2015

Major Subject: Mechanical Engineering

DEVELOPMENT, OPTIMIZATION, AND IMPLEMENTATION OF A VIBRATION BASED DEFECT DETECTION ALGORITHM FOR RAILROAD BEARINGS

A Thesis
By
AMY GONZALEZ

COMMITTEE MEMBERS

Dr. Constantine Tarawneh
Chair of Committee

Dr. Arturo Fuentes
Committee Member

Dr. Robert Jones
Committee Member

August 2015

ABSTRACT

Gonzalez, Amy, Development, Optimization, and Implementation of a Vibration Based Defect Detection Algorithm for Railroad Bearings. Master of Science (MS), August, 2015, 83 pp., 25 tables, 45 figures, 21 references.

Of the three main rail accident types in the United States, derailments are the most common. Studies have shown that derailments occurring above 25 mph are caused by equipment failures such as bearing failures. As a preventative measure, condition-monitoring systems are required to detect defective bearings in the field. Based on data compiled from multiple experiments of healthy and defective bearings at UTPA, an algorithm has been devised to identify bearing abnormalities. Vibration analysis techniques are utilized to potentially determine whether a bearing is defective and the defect type and size using the acquired vibration signatures. Implementation of a defect detection algorithm in the field can prevent catastrophic bearing failures from occurring; thus, reducing the chances of costly train derailments. This thesis summarizes the work done to develop an effective vibration-based defect detection algorithm that has been validated through field testing.

DEDICATION

The completion of this thesis would not have been possible without the unwavering love and support of my immediate and extended family, as well as my fiancé, Michael Diedrich. I would especially like to thank my mother, Mel, for always being around to support and motivate me through trying times. I would also like to dedicate this work to my brother, David, to show him that with hard work, dedication and commitment, one can achieve great success and fulfillment.

ACKNOWLEDGMENTS

I would first like to begin by thanking my research advisor, Dr. Constantine Tarawneh, for without whom, this thesis would not be possible. Thank you for your commitment and dedication to this work. You have truly supported and guided me through this long and rigorous journey.

Dr. Robert Jones, thank you for your involvement in this research. Your expertise in material science has been a great contribution to this research.

Dr. Arturo Fuentes, thank you for your guidance and commitment to my education. You are one of the most patient and caring professors I have met and I am so glad to have had the opportunity to work with you.

Special thanks to Dr. Stephen Crown for always managing to find humor during stressful times and providing your assistance whenever I requested your help. Having you as a professor has been an absolute privilege.

Additionally, I would like to thank Oscar and Ricky for helping me with my research. Especially Oscar, who happily took over responsibility of the testers without question or hesitation. You have been an enormous help. Thank you Thania and Joseph for helping me run field data. I know it was very time consuming, and I appreciate your contribution to this research. Thank you to the setup guys for all your hard work. I would also like to thank James L. Bantz, III, for his contribution to this research.

TABLE OF CONTENTS

Page

LIST OF TABLES

Page

LIST OF FIGURES

Page

CHAPTER I

BACKGROUND AND INTRODUCTION

More than five hundred and sixty railroads in the United States today operate over 140,000 rail miles to transport precious goods and cargo across the nation [1]. These goods and cargo range from coal and farm products to hazardous materials such as crude oil. As a result, many precautions and safety procedures have been regulated by the rail industry to prevent detrimental train accidents. Just last year, on April 30, a CSX train carrying crude oil derailed approximately fifteen rail cars in Lynchburg, VA [2]. Nearly 30,000 gallons of crude oil were leaked into a river near the downtown area, causing several derailed cars located along the river to catch fire [3]. Immediately following the accident, the City Manager declared an emergency and temporarily evacuated a portion of the downtown area [4]. No injuries were reported, and CSX was fined $361,000 as punishment for the derailment [3]. Although cause of the derailment is still under investigation, a study performed on derailment causes from 2001 to 2010 revealed bearing failures ranked second in derailments occurring at train speeds ranging from 25 to 80 mph at time of derailment [5]. Events such as these are the motivation behind the railroad bearing Defect Detection Algorithm presented in this thesis.

1.1 Tapered-Roller Bearings

In 2012, an estimated 19.7 billion tons of freight shipments were transported across the U.S. [6]. Weight capacities of railcars carrying these freight shipments range from 70 to 110 tons, depending on car type. The cargo load is mostly sustained by freight railcar components such as

axles, wheels, and bearings. However, the suspension component most susceptible to heavy cargo loads and high speeds is the tapered-roller bearing, located adjacent to the wheel, indicated in Figure 1. The tapered-roller bearing is comprised of three fundamental components: outer ring (cup), inner ring (cone), and roller (labeled in Figure 1).

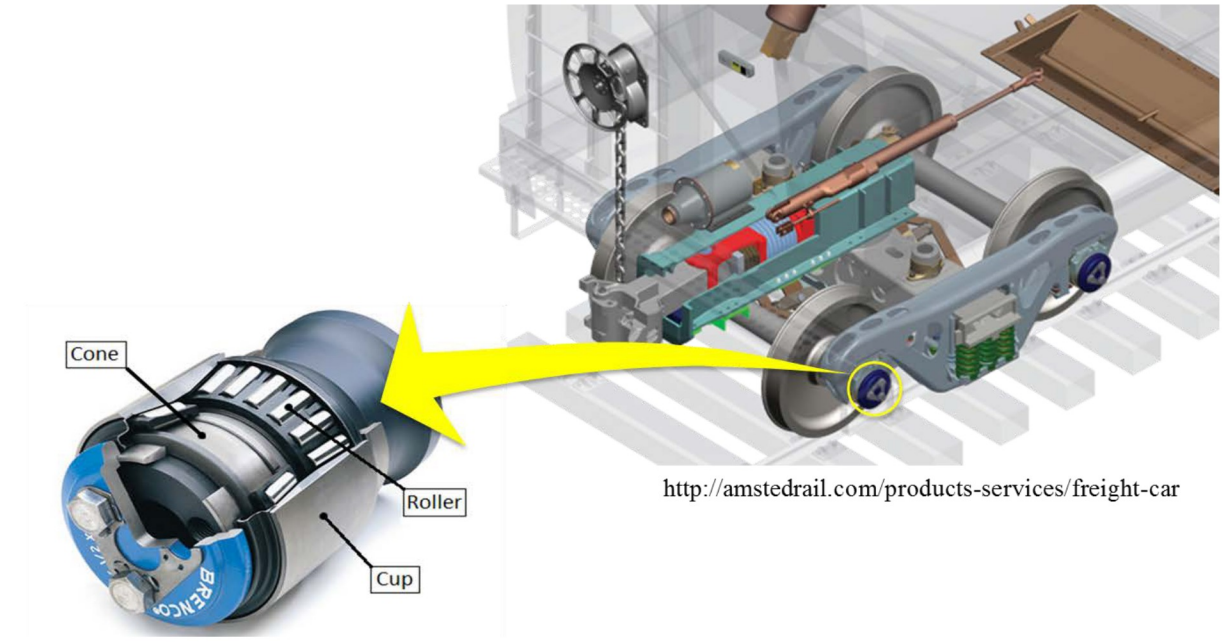

Figure 1 Typical tapered-roller bearing used on freight cars with annotated fundamental components (left) and its indicated location on a truck assembly (right).

The purpose of a bearing is to sustain heavy loads and reduce friction, however, when those functions are compromised, failure of the bearing ensues. Failure in a bearing refers to the bearing's inability to freely rotate, resulting in extreme frictional heating. Repercussions of an occurrence such as this are displayed in Figure 2.

Figure 2 Derailment caused by bearing failure, photographs courtesy of Amsted Rail.

Most instances of bearing failure are due to defects present within the bearing. According to researchers, defects fall into one of two categories: 'localized' or 'distributed' [7]. Localized defects include spalls, pits, and cracks, to name a few, whereas distributed defects involve surface roughness, water-etch – the result of water seeping into the bearing, causing grease degradation and metal to wear away –, geometric inconsistencies, etc. The effects of spalling, pitting, and water-etching on bearing components are displayed in Figure 3.

Rolling contact fatigue (RCF) is one of the most common causes of bearing failure, which can lead to spalling. Spalling typically occurs on rolling surfaces of a bearing due to the presence of subsurface inclusions. RCF causes micro-cracks to form around the inclusion. Under continued cyclic fatigue, the cracks begin to propagate towards the surface, causing metal to flake off, forming a cavity known as a 'spall'. The moment a spall initiates, metallic debris is introduced into the bearing lubricant, allowing the debris to become caught between the dynamic components of the bearing, forming dents and pits on raceway surfaces.

Figure 3 Photographs of a local cup defect exhibiting spalling and pitting (left) and water-etching on a cone raceway (right).

Ideally, nominal operating service life of a bearing should be at least two million rail miles until the bearing eventually succumbs to fatigue failure. Although fatigue cannot be prevented in a wheel bearing, precautions are performed so that impending failure of a bearing does not occur. Such precautions include bearing health monitoring systems.

1.2 Bearing Health Monitoring Systems

In the 1970s, most of the major railroads operating the nation's rail mileage went bankrupt, resulting in billions of dollars of deferred maintenance – necessary railroad maintenance that could not be afforded by railroads – which led to 'standing derailments' – falling of stationary railcars from track due to its poor maintenance [8]. Since Congress passed the Staggers Rail Act of 1980, railroads have increased their operating revenue significantly. Due to the increase in annual income, a proportional increase in investment has been made in rail safety and accident prevention. In 2014 alone, freight railroads spent $28 billion on rail infrastructure and equipment, contributing to the 80% decrease in accident rates since 1980 [9]. One major contribution to the decline in accident rates was implementation of condition monitoring systems.

In an effort to prevent derailments caused by equipment failures such as bearing failure, wayside detector systems located alongside the 140,000 working rail miles are implemented by the rail industry. Currently, the industry utilizes six detection systems which monitor wheels of passing trains and notify appropriate personnel of potential defects [10].

Prior to the invention of condition monitoring systems, railcar inspections were carried out manually with efficiency and effectiveness of the inspection varying depending on the experience of the railcar inspector. Although a train may be inspected to the best of an inspector's ability, unidentified defects would still occur due to limitations in the expertise of the inspector or conditions of the inspection. Recognizing this issue, the rail industry developed various condition monitoring systems such as wayside detector systems – systems located on or adjacent to tracks. In order to monitor the condition of railcar components, these detection systems utilize various sensors to measure temperature, sound, force, and railcar component geometry. In this section, two bearing condition monitoring systems will be discussed: hot box detector and trackside acoustic detection system.

1.2.1 Hot Box Detector

In 2014, over 60% of journal failure-caused derailments were a result of overheated bearings [11]. Of the bearings detected by hot box detectors (HBDs) from 2008 to 2012, 36.8% revealed signs of spalling and 24.5% were a result of water-etching, as provided by Amsted Rail. Hot box detectors, depicted in Figure 4, are wayside detection systems that use infrared sensors to measure the temperature emitted from bearings, wheels, axles and brakes. Bearings having operating temperatures greater than 94.4°C (170°F) above ambient are flagged by this system and trainmen are alerted to remove and disassemble these bearings for examination [12]. Disassembly and inspection of flagged bearings identified by HBDs have resulted in 40% of

non-verified bearings, according to data collected by Amsted Rail from 2001 to 2007. "A non-verified bearing is one that, upon disassembly and inspection, is found not to exhibit any of the commonly documented caused of bearing failure such as: spalling, water contamination, loose bearings, broken components, lubrication, damaged seals, etc." [12].

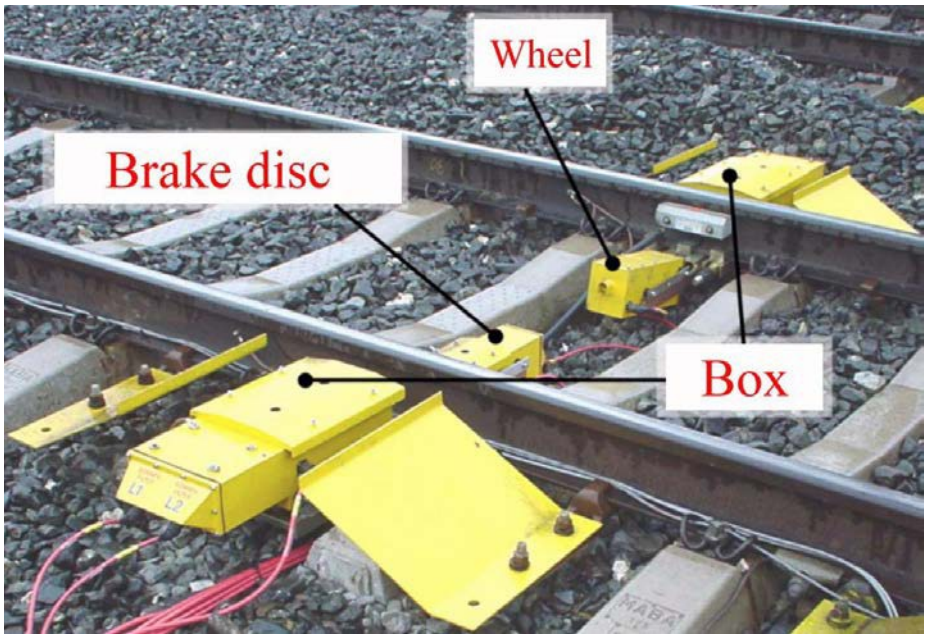

Figure 4 Photograph of a wayside hot box detector [13].

1.2.2 Trackside Acoustic Detection System

The trackside acoustic detection system (TADS), displayed in Figure 5, is comprised of a series of wayside microphones which monitor the sound emitted from bearing defects. In the early 1980s, acoustic bearing detection was developed to address the limitations of hot box detectors. Unfortunately, early implementations of these systems were unable to detect numerous defects. Once additional research was conducted, the acoustic bearing detectors were able to detect defects condemnable by the Association of American Railroads (AAR) standards.

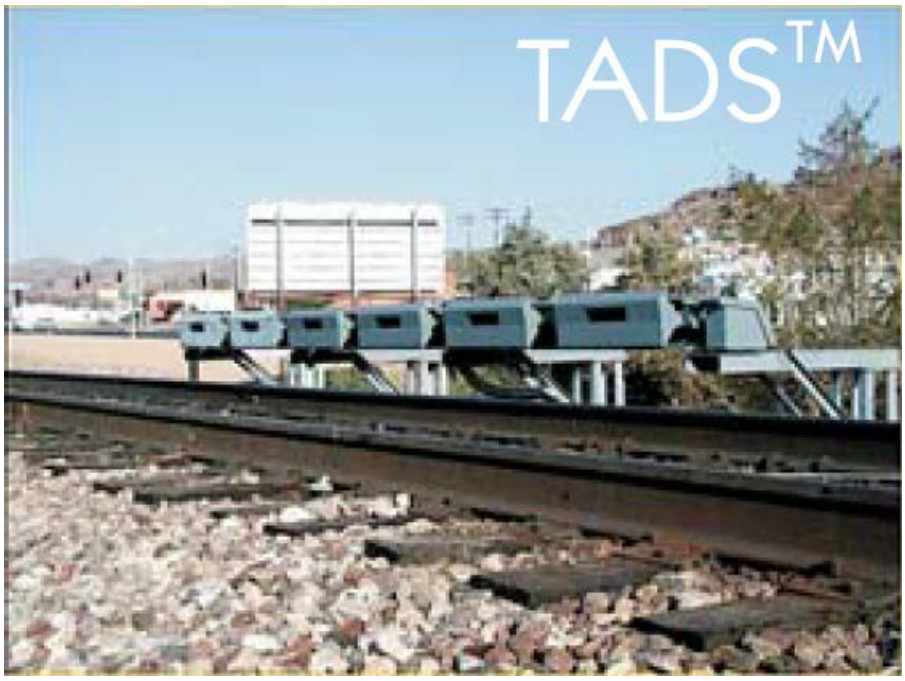

Figure 5 Photograph of a trackside acoustic detection system [15].

Although the original purpose of TADS™ was to detect smaller internal bearing defect having some significant risk, the system is currently able to detect large area defects such as 'growlers' – "…a term used by TTCI to describe the sound emitted from these large defects," [14]. In a study conducted by a TTCI (Transportation Technology Center, Inc.) researcher, twenty-seven of thirty-five detected bearings by TADS™ were considered growlers [14]. Nearly all of the twenty-seven defects termed 'growler' by TTCI revealed significant damage area, as shown in Figure 6. Although this system is able to detect high-risk bearing defects, if such defects are not removed within a reasonable amount of time, detrimental bearing failure may occur.

Figure 6 Photograph of a severe cone defect detected by TADS™ [14].

1.2.3 Current Research Developments at the University of Texas-Pan American

Due to the limitations of the wayside bearing condition monitoring systems currently implemented in the field, an onboard device which is capable of real-time, continuous bearing condition monitoring is sought. The ideal bearing monitoring device would measure the bearing's temperature, vibration, and applied load, which correspond to the measurements monitored by a hot box detector, trackside acoustic detector, and weighbridge – a section of track measuring the weight of a railcar –, respectively. If such a device existed, a method to analyze the acquired data would be needed.

The University of Texas-Pan American is currently conducting research on railroad bearings assembled with instrumented bearing adapters to monitor bearing health. Instrumentation includes thermocouples, accelerometers, and a strain gauge which measure bearing temperature, vibration, and load, respectively. Based on vibration data collected from multiple experiments of healthy and defective bearings, a bearing health monitoring algorithm was developed. This algorithm is able to determine whether a bearing is defective, identify the type of defect, and

estimate the size of the detected defect. A thorough description of the algorithm and its predecessor is provided in Chapter II.

CHAPTER II

BEARING DEFECT DETECTION ALGORITHM

The content provided in this chapter briefly describes a preliminary defect detection algorithm developed by Alvarado [16] and introduces an optimized algorithm built upon the foundation of the former. Both algorithms were developed based on analysis of vibration data acquired from healthy and defective railroad bearings. Differences between the two algorithms will be noted throughout section 2.2.

2.1 Preliminary Defect Detection Algorithm

In 2012, Alvarado [16] developed a preliminary defect detection algorithm capable of identifying the presence of defects within bearings while also determining the defect-type (local, distributed, or geometric), and estimating the size of the defect. The developed algorithm utilized vibration signatures gathered from healthy and defective bearings in laboratory experiments. Alvarado [16] explored several vibration analysis techniques prior to coming up with the technique used in her algorithm. Time- and frequency-domain analysis of the recorded vibration data form the basis for the developed algorithm. The preliminary defect-detection algorithm operates in a series of decision-making steps, expressed in Figure 7. The first step in the algorithm identified whether the bearing in question was defective. The second step determined whether or not the detected defect was local – a defect localized on a single bearing component (i.e., cup, cone, or roller). Depending on the outcome of the second step, the third

step in the algorithm either estimated the area and perimeter of the detected local defect, or compared the magnitude of the vibration to an established threshold, which would determine whether the defect was distributed or a false positive – a falsely detected healthy bearing.

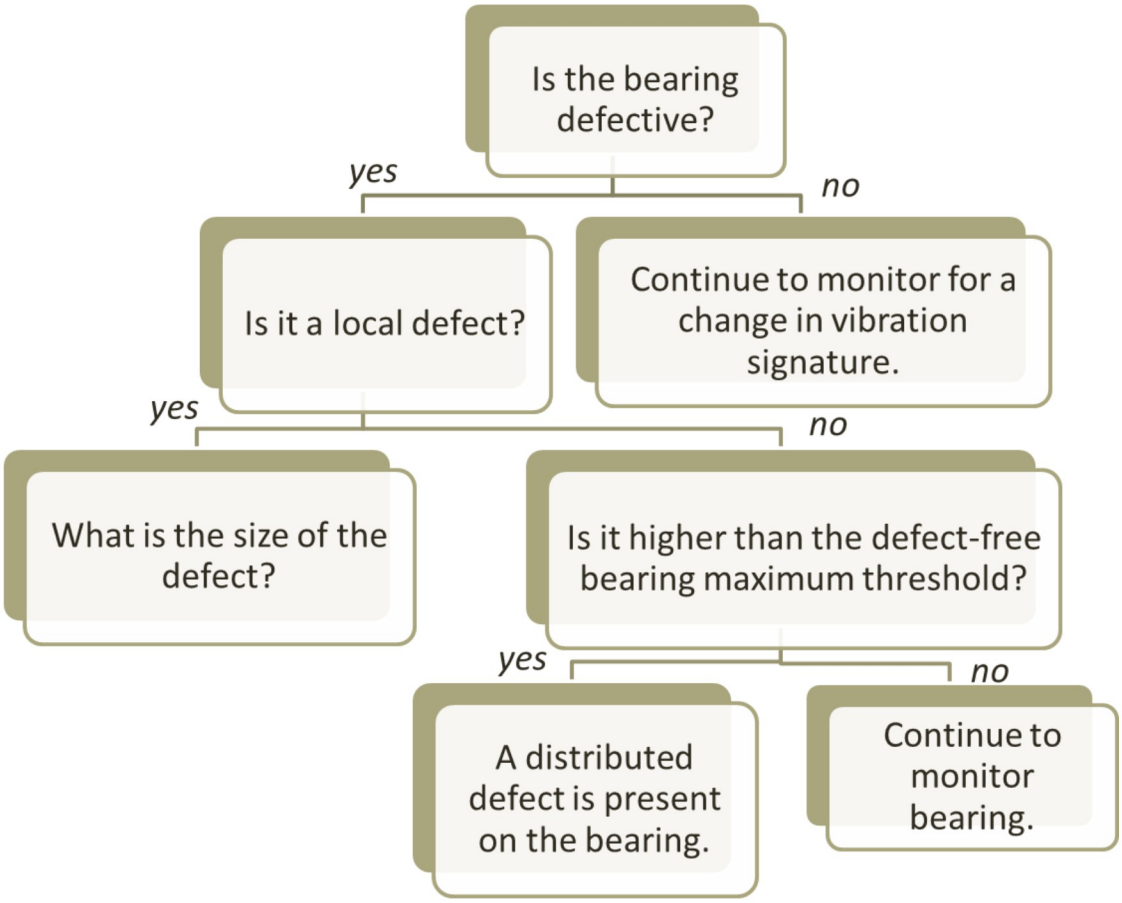

Figure 7 Flowchart of the defect-detection algorithm developed by Alvarado [16].

2.1.1 Step 1: Is the Bearing Healthy or Defective?

Step one of the preliminary defect-detection algorithm identified a bearing as defective or healthy by comparing the RMS value of the bearing in question to an RMS threshold. RMS, an acronym of root-mean-square, is a statistic used to measure the average of varying quantities ranging from negative to positive values. Because raw vibration signal collected from laboratory tested bearings is a sinusoidal time-domain signal, a statistical technique able to evaluate the data

was essential. The technique chosen by Alvarado [16] to quantify the signal was root-mean-square; its equation is given in Eq. 1.

$$RMS = \sqrt{\frac{1}{n}\sum_{i=1}^{n} {x_i}^2} \quad \text{Eq. 1}$$

The threshold was based on a thorough statistical analysis of healthy bearing vibration data. A series of thresholds were considered for step one with the notion that "The ideal initial threshold correlation should minimize the number of defect-free bearings erroneously categorized as defective, and minimize the number of defective bearings that are overlooked." [16]. The threshold accommodating the aforementioned requirement was the linear correlation equation of average defect-free bearing RMS data with 41% and 41.9% of defect-free and defective bearings falling above and below it, respectively [16]. The equation for the chosen RMS Threshold is provided in Eq. 2.

$$RMS\ Threshold = 0.0027 \times Speed\ [rpm] - 0.1508 \quad \text{Eq. 2}$$

2.1.2 Step 2: Is it a Local Defect?

Step two of the preliminary algorithm determined whether the defect identified in step one was local by implementing a method of tracking of fundamental defect frequencies within a power spectral density. Based on the magnitude of the tracked frequencies, Alvarado [16] developed the Magnitude Criterion presented in Eq. 3. The Magnitude Criterion compared the magnitude of each fundamental defect frequency to the sum of the three defect frequency magnitudes, outputting a percentage. The highest defect frequency magnitude with a percentage of 50% or greater indicated a defect localized on that component. However, if the percentage of the defect frequency was less than 50%, then the bearing either contained a distributed defect or was defect-free (evaluated in step three).

$$\frac{M_{cup,cone,roller}}{M_{cup} + M_{cone} + M_{roller}} \times 100 \geq 50\% \quad \text{Eq. 3}$$

2.1.3 Step 3: What is the Severity of the Defect?

Depending on the outcome of step two, step three of the proposed preliminary algorithm did one of the two sub-steps: estimate the size of the identified local defect, or determine if the bearing contained a distributed defect or was healthy. If a local cone defect was identified in step two of the algorithm, then estimations of the defect area and perimeter were predicted utilizing Eq. 4 and Eq. 5, respectively. If a local cup defect was identified, then the area and perimeter were estimated with Eq. 6 and Eq. 7, respectively.

$$A = \frac{RMS - b_A}{a_A}$$
$$a_A = 0.0029x - 0.4580$$
$$b_A = 0.0024x - 0.4339$$
$$A: Area$$
$$x: speed\ [rpm] \quad \text{Eq. 4}$$

$$P = \frac{RMS - b_P}{a_P}$$
$$a_P = 0.0007x - 0.0966$$
$$b_P = 0.0018x - 0.3727$$
$$P: Perimeter$$
$$x: speed\ [rpm] \quad \text{Eq. 5}$$

$$A = \frac{-d_A + \sqrt{{d_A}^2 - 4c_A(e_A - RMS)}}{2c_A}$$
$$c_A = 1 \times 10^{-5}x^2 - 0.0053x + 1.0256$$
$$d_A = -(1 \times 10^{-5}x^2 - 0.0068x + 1.2928)$$
$$e_A = 3 \times 10^{-6}x^2 - 0.0004x + 0.2859$$
$$A: Area$$
$$x: speed\ [rpm] \quad \text{Eq. 6}$$

$$P = \frac{-d_P + \sqrt{{d_P}^2 - 4c_P(e_P - RMS)}}{2c_P}$$
$$c_P = 9 \times 10^{-7}x^2 - 0.0003x + 0.0437 \quad \text{Eq. 7}$$

$$d_P = -(4 \times 10^{-6}x^2 - 0.0018x + 0.2946)$$
$$e_P = 6 \times 10^{-6}x^2 - 0.0014x + 0.4258$$
$$P: Perimeter$$
$$x: speed\ [rpm]$$

Determining whether the bearing contains a distributed defect or is a false positive is evaluated by comparing the RMS of the bearing in question to a second threshold, referred to as the Maximum Threshold, represented in Eq. 8, and established from the maximum RMS values of healthy bearings at various speeds. If the RMS value was greater than the Maximum Threshold, then the detected defect was distributed. If the RMS value is less than the threshold, then the bearing is classified as defect-free.

$$Maximum\ Threshold = 0.0033 \times Speed\ [rpm] + 1.1936 \quad \text{Eq. 8}$$

2.2 Optimized Defect Detection Algorithm

The optimized defect detection algorithm depicted in Figure 8 is constructed to identify the presence of a defect within a bearing, determine the defect type, and estimate the defect size in terms of area. In a field setting, the algorithm will not initiate unless a trigger occurs. Triggers include a bearing operating temperature greater than 200°F (~ 93°C) or a train operating at a speed of at least 40 mph (~ 64.4 km/h). Subsequent to algorithm initiation, a data acquisition system will collect 4 seconds of vibration data at a sampling rate of 5 kHz (20,000 data points) from an accelerometer affixed to the bearing's adapter. Once data is collected, the root-mean-square (RMS) will be calculated, outputting a single g value. A description of each level within the algorithm is given hereafter.

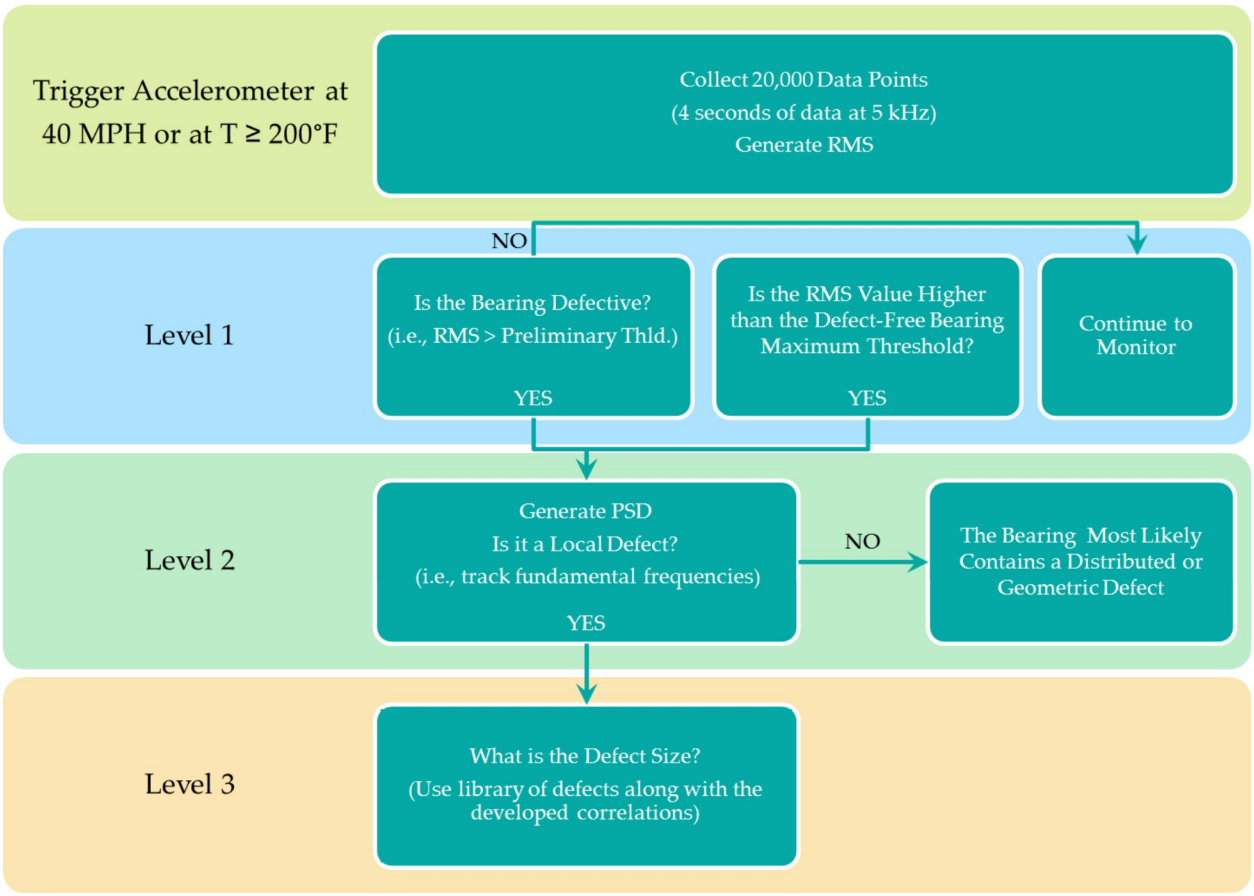

Figure 8 Flowchart of the optimized railroad bearing defect-detection algorithm.

2.2.1 Level 1: Is the Bearing Defective?

Level 1 of the algorithm determines whether a bearing is defective or defect-free (healthy). To this end, two speed-dependent thresholds were produced from a library of defect-free bearing vibration signatures acquired through laboratory testing. The RMS value calculated prior to Level 1 is compared to these two thresholds. A description of the two thresholds follows.

2.2.1.1 Average Threshold. The preliminary threshold was selected following a statistical examination of various possible thresholds. These thresholds are based on a correlation of speed and mean defect-free bearing RMS values collected from sixty-two experiments. The acquired data is plotted in Figure 9. Each data point in the figure is an average of RMS values collected at 17% and 100% of full load. The testing speeds ranged from 25 mph (~40 km/h) to 85 mph

(~137 km/h), and the loads included 17% and 100% of full load for class F or K bearings (full load corresponds to 34.4 kips or 153 kN per bearing as per AAR standards).

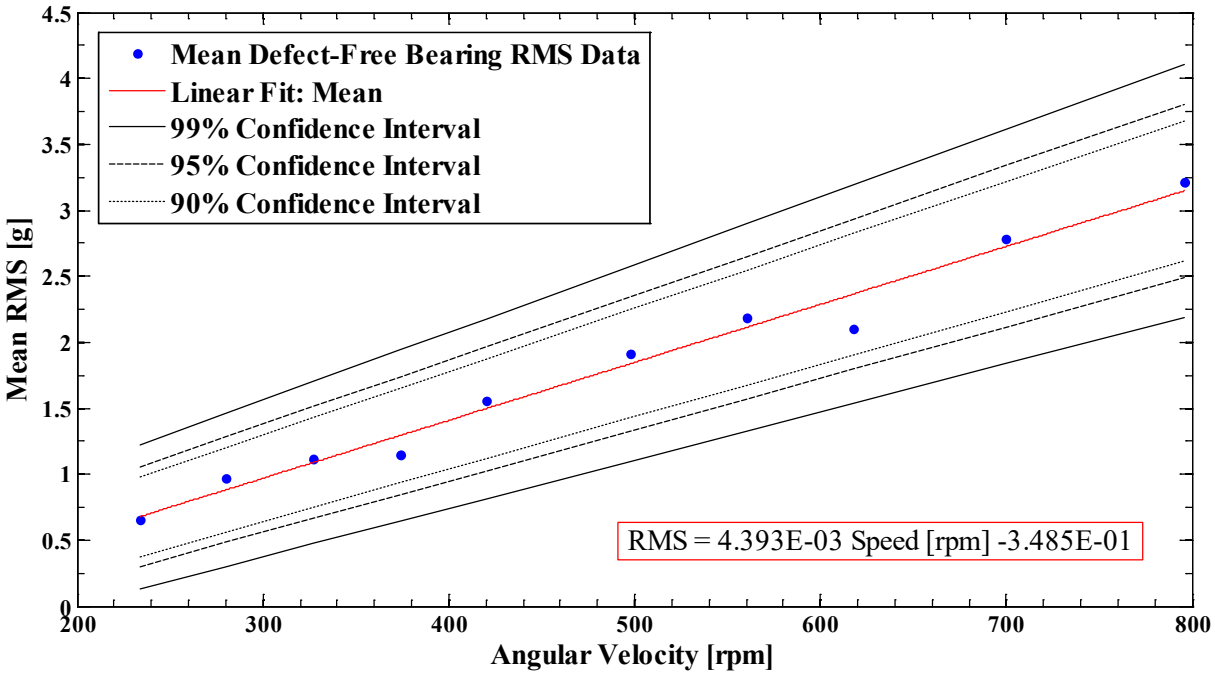

Figure 9 Plot of mean defect-free bearing RMS values correlated to angular velocity which includes a linear fit of the data with 90%, 95%, and 99% confidence intervals.

Several possible thresholds were explored based on the following statistics: μ, $\mu \pm \frac{1}{2}\sigma$, $\mu \pm \sigma$, and upper and lower bounds of the 90%, 95%, and 99% confidence intervals for the mean RMS in Figure 9. The confidence intervals represent a proportion of samples which contain the true mean of the population. The variables μ and σ represent the mean and standard deviation of defect-free bearing RMS values for each speed, respectively. All eleven possible thresholds and their corresponding correlations are displayed in Figure 10.

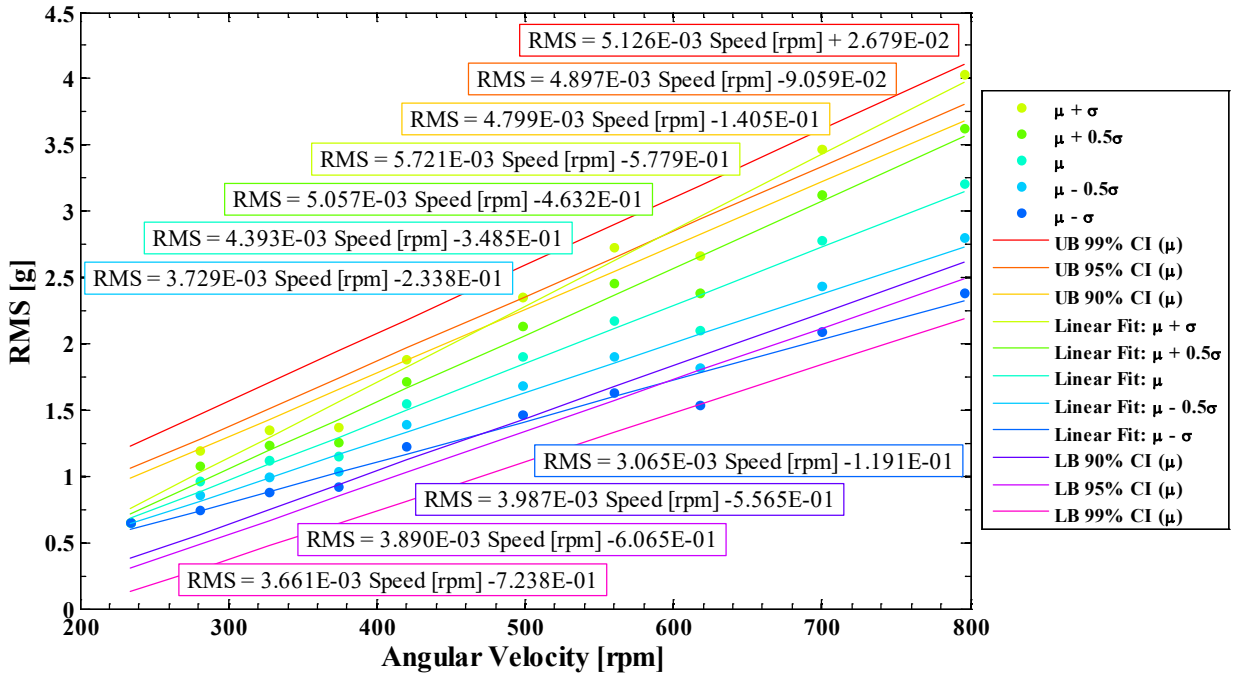

Figure 10 Possible speed-dependent statistical thresholds and their corresponding equations.

Following Alvarado's strategy (refer to section 2.1.1), the ideal preliminary threshold should minimize the number of false positives while also limiting the amount of false negatives. In other words, minimize the number of healthy bearings incorrectly identified as defective, and limit the number of unidentified defective bearings. To determine which threshold meets this criterion, all defect-free and defective bearing RMS values were compared to each threshold. The results are summarized in Table 1.

Table 1 Percentages of defect-free and defective bearing RMS values that fall above and below possible threshold correlations, respectively.

Possible Threshold	Defect-free Bearing RMS Values Above Possible Threshold	Defective Bearing RMS Values Below Possible Threshold
Upper Bound 99% CI (μ)	13.8%	33.2%
Upper Bound 95% CI (μ)	19.3%	27.4%
Upper Bound 90% CI (μ)	21.8%	26.6%
μ + σ	26.8%	23.5%
μ + ½ σ	33.9%	20.5%
μ	43.8%	15.8%
μ - ½ σ	52.1%	11.6%
μ - σ	61.0%	8.5%
Lower Bound 90% CI (μ)	65.3%	6.9%
Lower Bound 95% CI (μ)	72.6%	6.2%
Lower Bound 99% CI (μ)	87.9%	3.5%

Unlike the average-based RMS Threshold chosen by Alvarado [16] in section 2.1.1, the average threshold in Table 1 did not meet the desired criterion. Rather, the top three best possible thresholds with the lowest percentages of false positives and compromising percentages of false negatives were the upper bounds of the 90%, 95%, and 99% confidence intervals for the mean defect-free bearing RMS values. Despite the upper bound of the 99% confidence interval threshold having the least number of defect-free bearing RMS values falling above it, almost a third of defective bearings were overlooked. As a result, the number of possible thresholds decreased to two: upper bounds of the 90% and 95% confidence intervals. Because the difference in percentages listed in Table 1 for these two thresholds was minimal, the better of the two was chosen – the upper bound of the 95% confidence intervals for the mean defect-free bearing RMS values. The preliminary threshold equation for Level 1 is given in Eq. 9.

$$RMS_{Prelim.Thld.} = 4.879 \times 10^{-3} \times Speed\ [rpm] - 9.059 \times 10^{-2} \quad \text{Eq. 9}$$

If the RMS value calculated prior to Level 1 is greater than the Preliminary Threshold, then the bearing is categorized as defective and the algorithm will proceed to Level 2. Conversely, if the RMS value is below the initial threshold, then the bearing is considered defect-free, and data

collection resumes according to the algorithm triggers discussed earlier. In a field setting, if the RMS value of the bearing in question is identified as possibly defective when compared to the Preliminary Threshold RMS value, then it is highly recommended that data be collected eight times daily in order to properly track the condition of the bearing.

2.2.1.2 Maximum Threshold. The second threshold in Level 1 is the Maximum Threshold. This threshold was established with the criterion that 100% of all bearings with an RMS value above it would be defective. The Maximum Threshold is based on a correlation between the maximum defect-free bearing RMS values and the speed. Originally, the linear fit equation generated by the positive linear correlation between maximum RMS and speed, displayed in Figure 11, was to be the Maximum Threshold. Unfortunately, approximately 2% of defect-free bearing RMS values from the vibration library fell above this threshold. Rather than simply shifting the linear correlation line of the maximum RMS data in Figure 11 to encompass all maximum RMS values, the upper bound of the 45% confidence intervals shown in Figure 11 was utilized. The confidence intervals are based on the proportion of samples, from which the maximum RMS values were acquired, that contain the true maximum of the defect-free bearing RMS population.

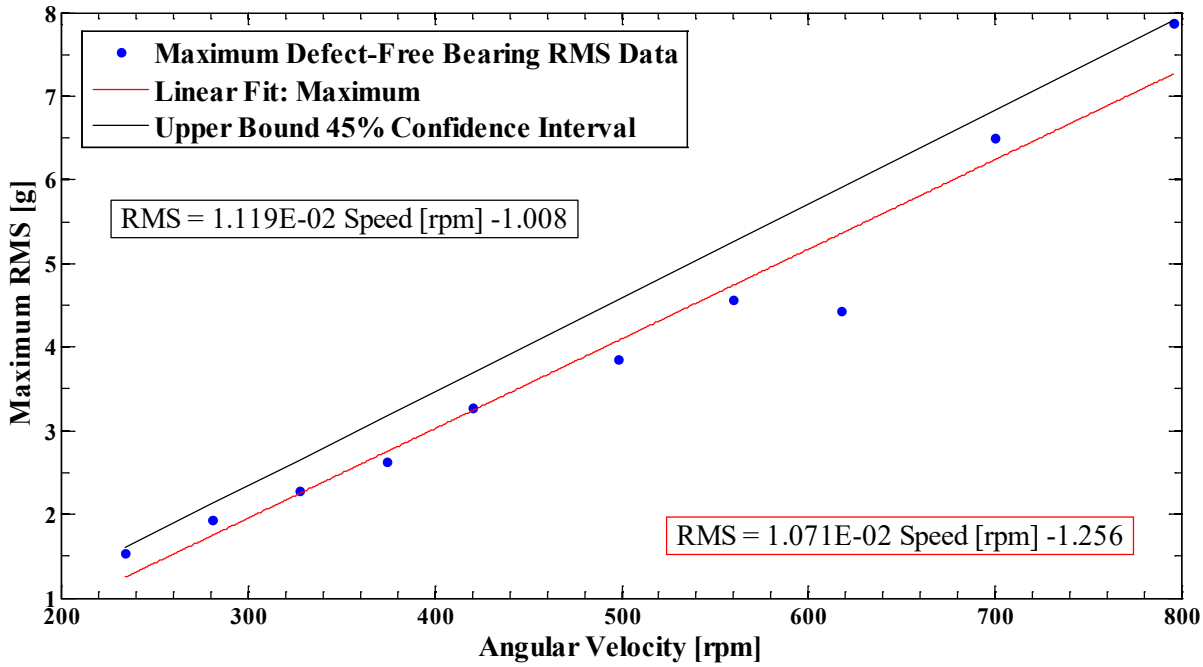

Figure 11 Plot of maximum defect-free bearing RMS values correlated to angular velocity including linear correlation line and upper bound of the 45% confidence intervals.

Employing this statistic as the Maximum Threshold, 100% of all bearings with an RMS value above it have been found to be defective in laboratory testing. In a field setting, if the RMS value calculated prior to Level 1 is greater than the Maximum Threshold, it is recommended that data be collected twelve times daily in order to properly track the bearing condition and the defect severity. The equation of the Maximum Threshold is given in Eq. 10.

$$RMS_{Max.Thld.} = 1.119 \times 10^{-3} \times Speed\ [rpm] - 1.008 \qquad \text{Eq. 10}$$

2.2.2 Level 2: What is the Defect Type?

In this level, the algorithm determines the type of defect (local or distributed/geometric) present within the detected defective bearing utilizing frequency-domain analysis, which consists of tracking rotational frequencies in a power spectral density (PSD) plot, where a PSD is the square of the magnitudes in the frequency domain, as shown in Eq. 11.

$$PSD = \int_{-\infty}^{\infty} |X(f)|^2 df \quad \text{Eq. 11}$$

In the laboratory, calculation of the PSD was executed in MATLAB® primarily using the $fft(X, n)$ function to generate an n-point discrete Fourier transform (DFT) – computed with a fast Fourier transform (FFT) algorithm – and then squaring the amplitudes of the frequency spectrum [17]. The data acquisition (DAQ) in the laboratory was programmed to sample data at 5.12 kHz and record 4 seconds of data, generating a sample length of 20480 data points. Due to sensor-to-hardware-to-software compatibility, 5.12 kHz was the nearest to 5 kHz the DAQ would allow. Because expedited processing time of the FFT was achieved when the sample length was a power of 2, 32768 points were used to generate the FFT, where 32768 was the next power of 2 more than 20480, which essentially zero padded the FFT. Due to the addition of 12288 trailing zeros to generate the FFT, the density of FFT bins increased, thus, accurately estimating the amplitude of significant frequencies within the spectrum.

The equations of the three fundamental tapered-roller bearing frequencies and three fundamental defect frequencies of interest are listed hereafter.

$$\omega_{cone} = \omega_o \quad \text{Eq. 12}$$

$$\omega_{cage} = \left(\frac{R_{cone}}{R_{cone} + R_{cup}}\right)\omega_{cone} \quad \text{Eq. 13}$$

$$\omega_{roller} = \left(\frac{R_{cone}}{D_{roller}}\right)\omega_{cone} \quad \text{Eq. 14}$$

$$\omega_{out} = 23\omega_{cage} \quad \text{Eq. 15}$$

$$\omega_{in} = 23\left(\omega_{cone} - \omega_{cage}\right) \quad \text{Eq. 16}$$

$$\omega_{rolldef} = \left(\frac{R_{cup}}{R_{roller}}\right)\omega_{cage} \quad \text{Eq. 17}$$

Eq. 12 – Eq. 17 are based on the rotational speed (ω_o) and geometry of a tapered-roller bearing, where R_{cone}, R_{cup} and R_{roller} represent the radii of the cone (inner ring), cup (outer ring), and roller components of the bearing, respectively, and the roller diameter represented as D_{roller}. The equations for each of the six fundamental frequencies are based on the work done by Tarawneh *et al* where the six frequencies were used to track roller misalignments in temperature trending bearings [18]. The three fundamental rotational frequencies are the cone/axle (ω_{cone}), cage (ω_{cage}) and roller (ω_{roller}), whereas, the three fundamental defect frequencies are derived from those bearing component frequencies and are the cup (ω_{out}), cone (ω_{in}), roller defect ($\omega_{rolldef}$).

Looking at Figure 12, one can observe that each defect type, including the absence of a defect, has unique characteristics within the frequency spectrum. For instance, a healthy bearing exhibits little to no peaks throughout the spectrum, and any peaks present in the frequency plot are relatively low in magnitude, as illustrated in Figure 12 (a). A bearing with a cup defect shows a high-magnitude cup defect frequency (ω_{out}) along with high-magnitude harmonics, as can be seen in Figure 12 (b). Similarly, a bearing containing a cone defect exhibits a high-magnitude cone defect frequency (ω_{in}) as well as high-magnitude harmonics, as shown in Figure 12 (c). Another characteristic observed in the cone-defect frequency spectrum are the numerous evenly-spaced, high-magnitude peaks, which are a cone/axle frequency (ω_{cone}) apart. In comparison to the cup- and cone-defect frequency spectrums, the roller defect spectrum contains a low-magnitude roller defect frequency in addition to low-magnitude harmonics, as depicted in

Figure 12 (d). Comparable to the cone-defect frequency spectrum, the roller-defect frequency spectrum also has numerous evenly-spaced peaks which are a cage frequency (ω_{cage}) apart.

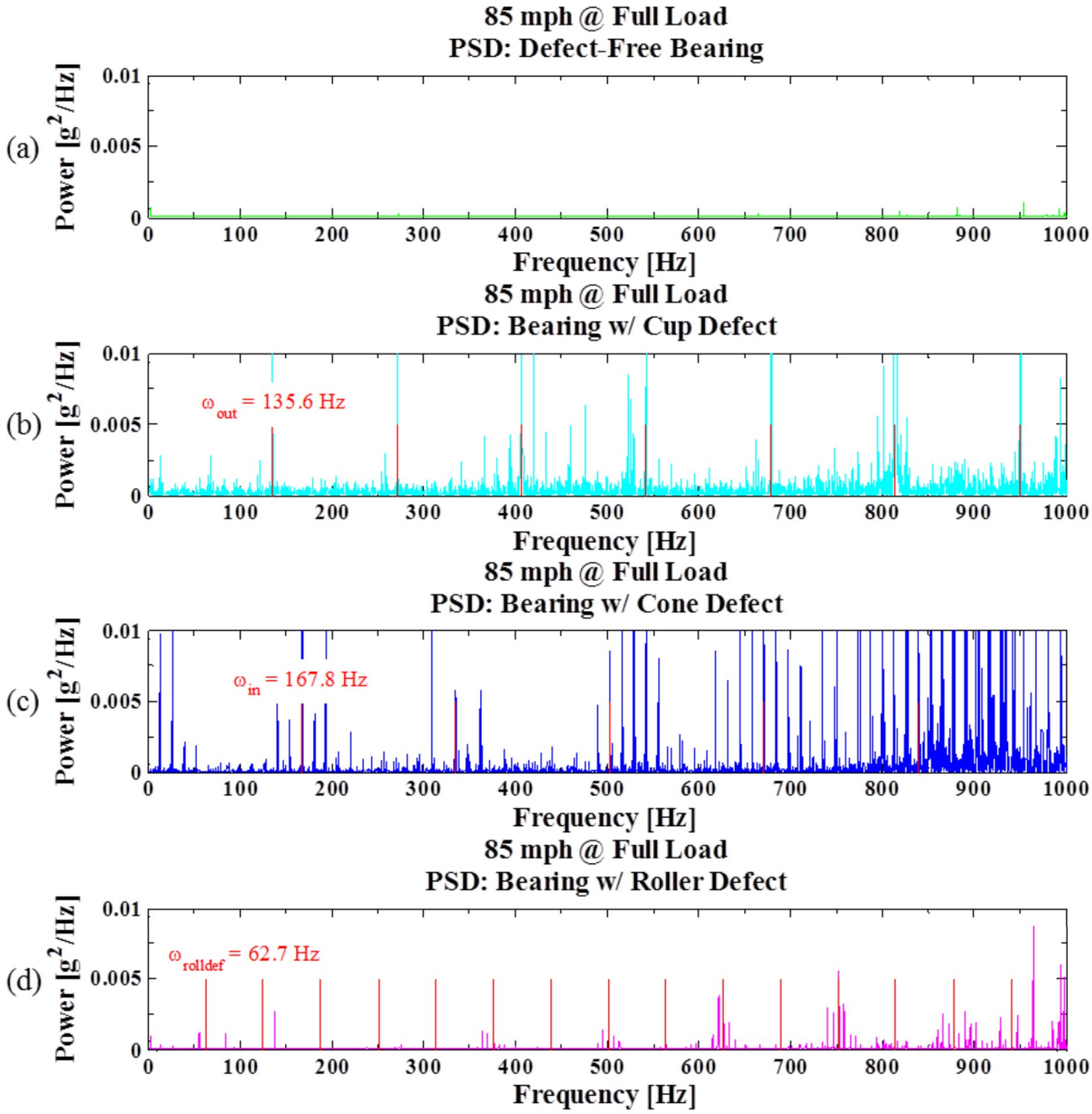

Figure 12 Frequency spectrum plots (0 – 1000 Hz) of (a) a defect-free bearing, (b) outer ring defect, (c) inner ring defect, and (d) a roller defect.

Due to the uniqueness of each power spectrum displayed in Figure 12, the defective component within a bearing can be identified by calculating the normalized defect energy (NDE), a numerical method developed by Alvarado [16], for each defect type and determining

which of the three NDEs is greater. Normalized defect energy refers to the summation of areas under a specified defect frequency (cup, cone, or roller) and its harmonics within the PSD, divided by the total number of harmonics within a defined range. However, to determine the NDE of a cup, cone and roller defect, one must first identify the actual fundamental defect frequencies. During laboratory testing, it was observed that the calculated frequencies were slightly shifted from the actual defect frequencies (see Figure 13). This occurrence was also noted by Alvarado [16] and Maldonado [19]. The shifting of these frequencies is the result of two possible scenarios: slipping or skidding of rollers within the bearing cone assembly during operation, and/or variations in the geometric tolerances of the bearing components. Note that the calculated frequencies of Eq. 12 – Eq. 17 use the bearing component measurements specified in the manufacturing drawings, but these measurements can vary based on the manufacturing tolerances.

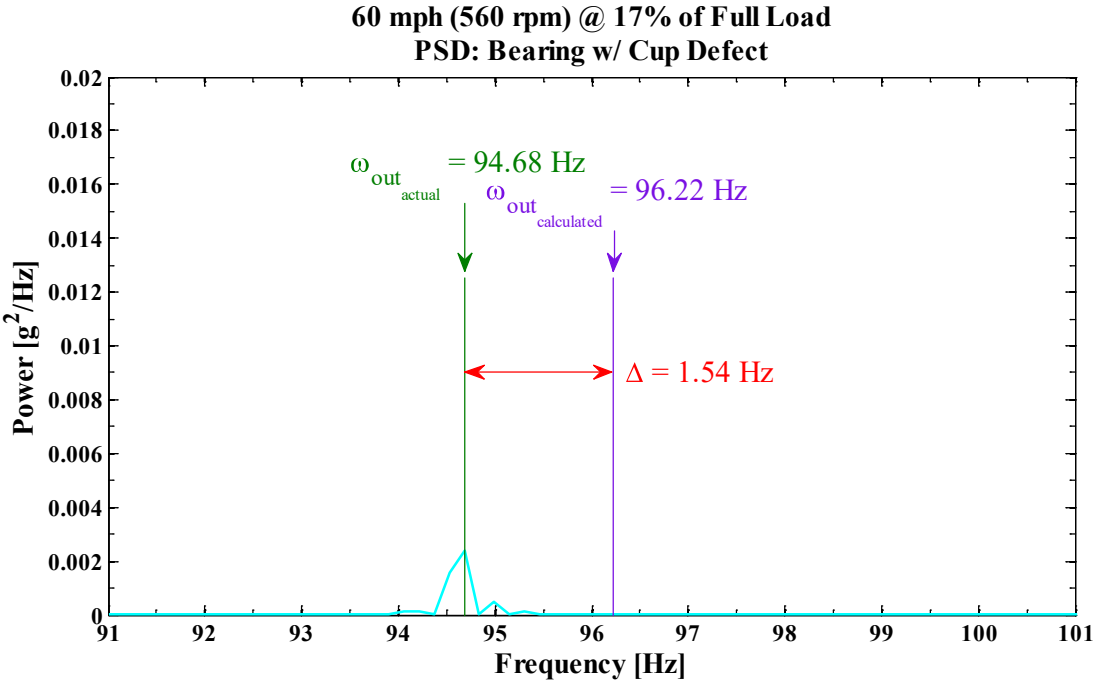

Figure 13 Power spectrum plot illustrating shifting of the cup defect frequency.

To compensate for this frequency shifting, a hunting range (h_r) is incorporated into Level 2 analysis to determine the location of the actual defect frequency. This range is a function of the resolution, Eq. 18, of the spectrum, and varies based on the angular speed (ω_o) of the bearing, as shown hereafter:

$$Resolution = \frac{Sampling\ frequency}{\#\ of\ points\ per\ FFT} \quad \text{Eq. 18}$$

Low Speed: $\omega < 350\ rpm, h_r = \pm Resolution \times 6$

Medium Speed: $350\ rpm \leq \omega < 610\ rpm, h_r = \pm Resolution \times 10$

High Speed: $610\ rpm \leq \omega, h_r = \pm Resolution \times 15$

These ranges were established by manually hunting for the actual defect frequencies from numerous laboratory tests run at various speeds. Once the actual defect frequency is found, the normalized defect energy can be computed. The equations used to calculate normalized defect energy for each defect frequency are represented in Eq. 21 – Eq. 23. Because shifting can occur throughout the spectrum, as illustrated in Figure 14, an integration range (i_r, Eq. 20) is set in place to capture most, if not all, harmonics of the fundamental defect frequency up to 1000 Hz, where shifting beyond this frequency became greater than the appointed integration range, as demonstrated in Figure 14. The *floor* function in Eq. 19 outputs the largest number of harmonics for a specified defect frequency within the desired frequency range.

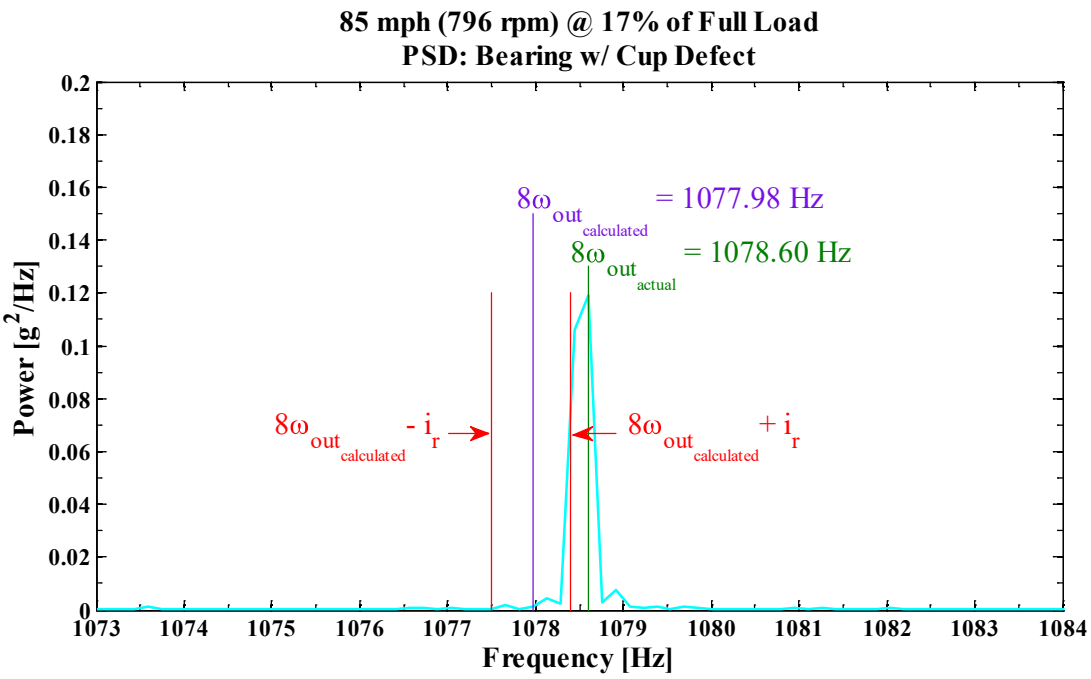

Figure 14 Power spectrum depicting shifting of the 8th harmonic of ω_{out}.

$$n = floor\left(\frac{defined\ frequency\ range}{defect\ frequency}\right) \quad \text{Eq. 19}$$

$$i_r = Resolution \times 3 \quad \text{Eq. 20}$$

$$NDE_{cup} = \frac{\sum_{i=1}^{n}\int_{i\omega_{out}-i_r}^{i\omega_{out}+i_r}|X(f)|^2 df}{n} \quad \text{Eq. 21}$$

$$NDE_{cone} = \frac{\sum_{i=1}^{n}\int_{i\omega_{in}-i_r}^{i\omega_{in}+i_r}|X(f)|^2 df}{n} \quad \text{Eq. 22}$$

$$NDE_{roller} = \frac{\sum_{i=1}^{n}\int_{i\omega_{rolldef}-i_r}^{i\omega_{rolldef}+i_r}|X(f)|^2 df}{n} \quad \text{Eq. 23}$$

Based on the foundation of the Magnitude Criterion developed by Alvarado [16] (refer to section 2.1.2), in order to determine the defective component (cup, cone, or roller) present within the identified defective bearing, the highest normalized defect energy of the three defect types ($NDE_{cup,cone,roller}$) must be greater than or equal to 50% of the sum of all three normalized defect energies, as shown in Eq. 24. If the normalized defect energy of one of the three bearing components is greater than 50% of the sum of all three normalized defect energies, then the

identified defective bearing contains a localized defect on that corresponding component. If this is not the case, then the defective bearing may contain a geometric or distributed defect, or the bearing is a falsely detected healthy bearing (not very common). A geometric defect is any geometric inconsistency in the bearing components' manufacturing tolerances, and a distributed defect is spalling that has occurred on two or more of the rolling contact surfaces of the bearing components.

$$\frac{\max(NDE_{cup,cone,roller})}{NDE_{cup} + NDE_{cone} + NDE_{roller}} \times 100 \geq 50\% \qquad \text{Eq. 24}$$

2.2.3 Level 3: What is the Defect Size?

If the presence of a local defect is detected in Level 2, then the area of the defect is estimated in Level 3. The predicted defect size is an estimation based on developed relationships between RMS values and their corresponding defect areas. These correlations were established strictly for cup and cone spalls. Because roller spalls typically initiate as a result of a neighboring defective component (cup and/or cone), and occur on multiple rollers within a cone assembly, a relationship was not established. When correlating RMS versus cup defect size, an exponential relationship was observed, as represented in Figure 15. Unlike the cup defect correlation, the relationship between RMS and cone defect area proved to be more linear, as illustrated in Figure 16.

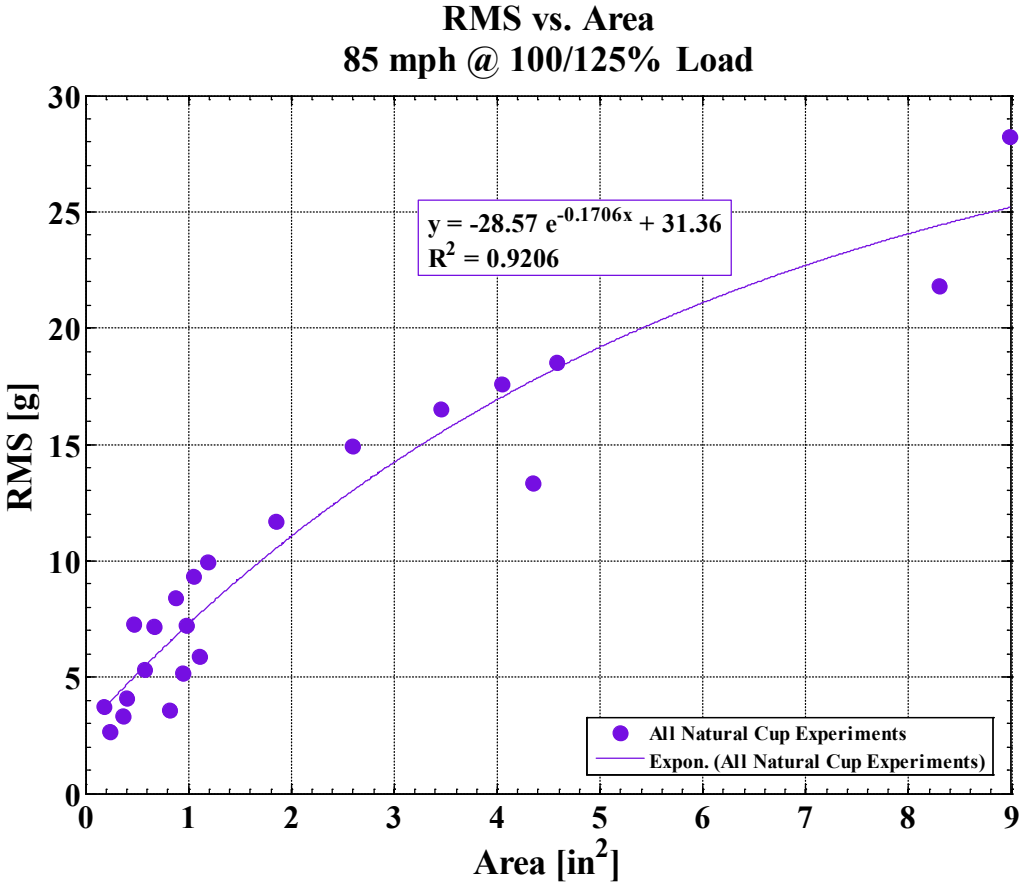

Figure 15 Cup defect size correlation at 85 mph and 100/125% of full load.

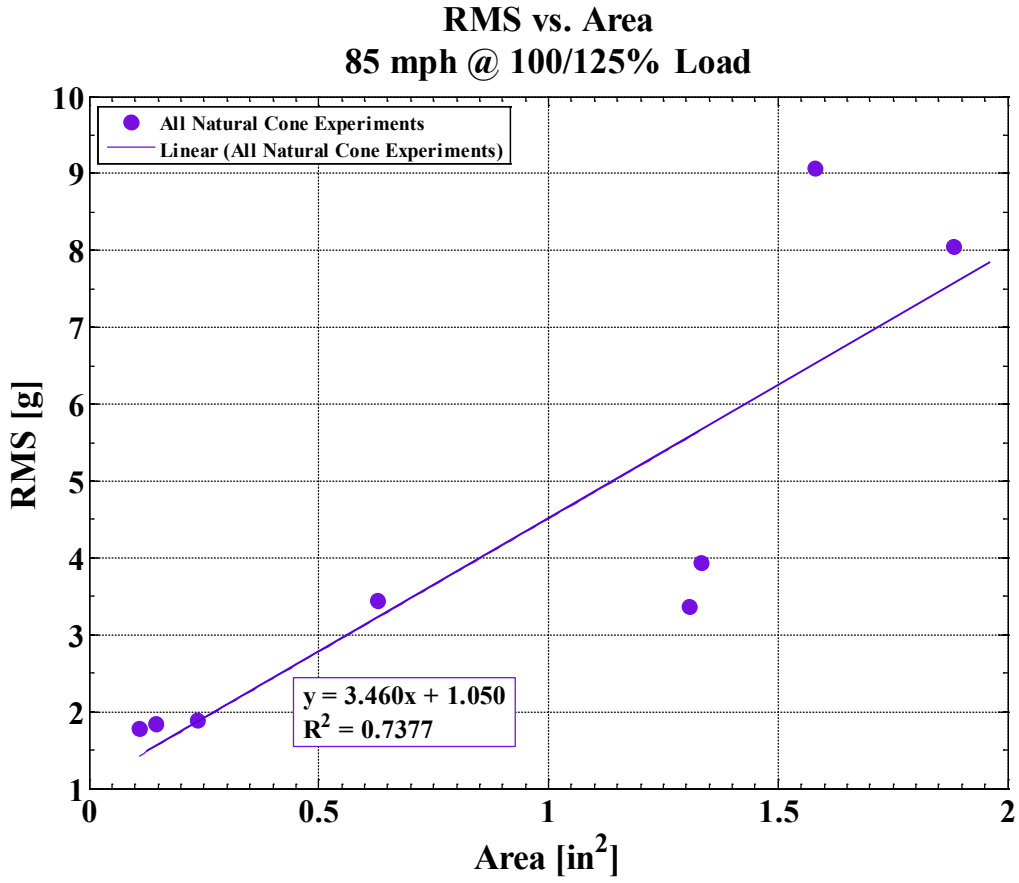

Figure 16 Cone defect size correlation at 85 mph and 100/125% of full load.

The data used to devise the above correlations was acquired entirely from running bearing components that developed spalls during their field service life, and/or spalls that initiated as a result of subsurface inclusions. Laboratory data collected from running bearing components that contained manmade defects that were created by a Dremel® tool were not used in the above correlations. A majority of the data from both plots, Figure 15 and Figure 16, were collected from cup and cone service life tests, which were run at 85 mph and 100% of full load to expedite spall initiation. Although both correlations were obtained while tests ran at full load, the correlations can be used for data collected at 17% of full load. Previous laboratory experiments have shown minimal variations between the two loading conditions.

CHAPTER III

EXPERIMENTAL SETUP AND INSTRUMENTATION

The development of an algorithm capable of monitoring bearing health and detecting defects or geometric inconsistencies within the bearing requires thorough analysis of vibration signatures from multiple bearing conditions ranging from a perfectly healthy bearing to a bearing containing multiple defects. In order to conduct this analysis, a database of vibration data compiled from multiple experiments performed with healthy and defective railroad tapered-roller bearings has been and continues to be assembled at UTPA (University of Texas-Pan American). The types of defects contained within test bearings include local (defects localized on a single bearing component), distributed (asperities on multiple bearing components), and geometric defects. Assessments of these bearings were conducted in a laboratory setting where field conditions were replicated. The experimental setup employed to recreate a field environment is as follows:

3.1 Four-Bearing Tester Setup

Laboratory testing of railroad bearings was performed on two dynamic four-bearing test rigs at UTPA. The dynamic testers are able to accommodate four tapered-roller bearings of one of the following classes: Class E (6 × 11 in.), Class F (6 ½ × 12 in.), Class G (7 × 12 in.), and Class K (6 ½ × 9 in.), which are mounted on a custom test axle coupled to a drive motor by a pair of appropriately sized pulleys. Although both testers are capable of testing these different bearing

classes, only data collected from Class F and K bearings was used for the development of the defect detection algorithm presented in this thesis. Each bearing tested in the laboratory is assembled using AAR (Association of American Railroads) Standards. The assembled bearings are then mounted onto the test axle by means of a 500-ton hydraulic press. Following the test rig assembly, bearings were labeled B1 to B4 in ascending order from the pulley side to the end cap side, as indicated in Figure 17: Photograph of Tester 1, a four-bearing dynamic test rig with a fixed-speed motor.

Because Tester 1, shown in Figure 17, is operated by a fixed-speed motor, different pulley sizes are required to change the test speed. Utilizing the four pulley sizes available in the laboratory, the test axle is able to rotate at angular velocities of 498, 562, 618, and 794 rpm, which correspond to train speeds of approximately 53, 60, 66, and 85 mph, respectively. Unlike Tester 1, Tester 2, depicted in Figure 18, utilizes a variable-speed drive motor which has a maximum speed of 85 mph based on the largest pulley size available in the laboratory, and is controlled by a variable frequency drive. Hence, Tester 2 is able to provide testing speeds ranging anywhere from 0 to 85 mph. Table 2 lists the ten speeds that were used to run the experiments for this study. For cooling, both testers employed two large industrial fans to provide cross-flow over the test axle, which simulated the airflow created by a moving train. Additionally, Tester 2 is enclosed within a temperature-controlled environmental chamber capable of producing ambient temperatures ranging from -40°C to 50°C. However, the majority of experiments were carried out in ambient temperatures ranging from 20 to 30°C.

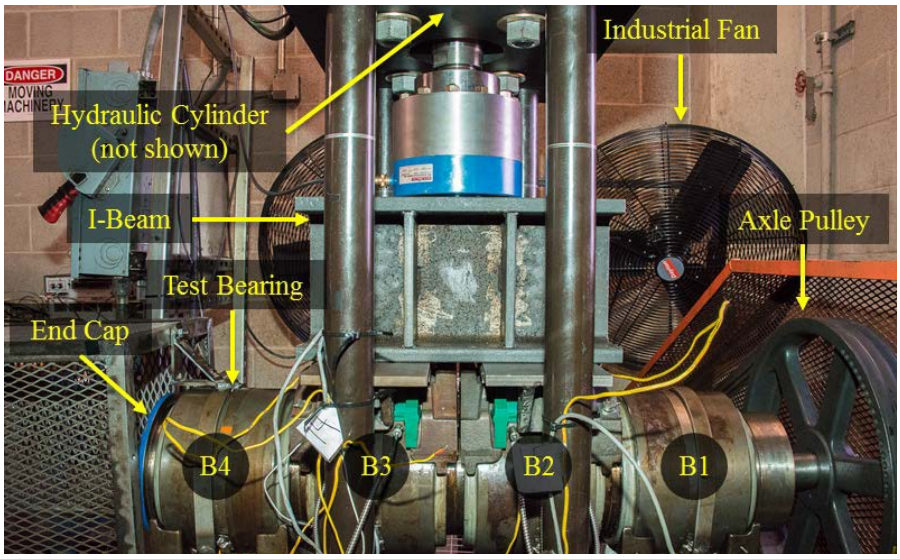

Figure 17: Photograph of Tester 1, a four-bearing dynamic test rig with a fixed-speed motor.

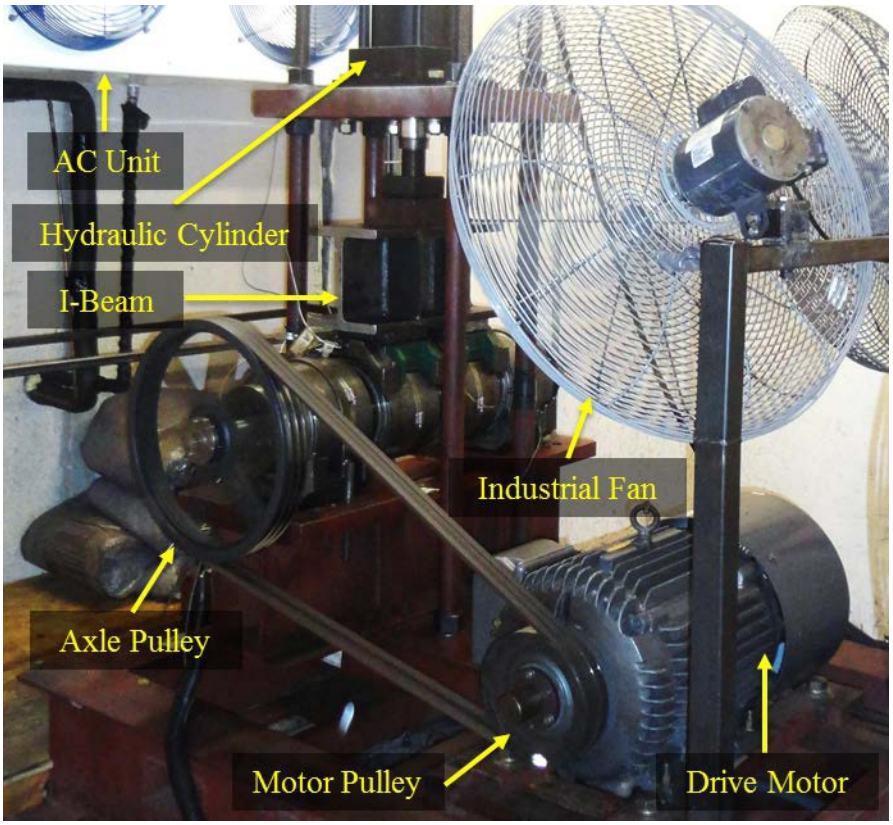

Figure 18: Photograph of Tester 2, a four-bearing dynamic tester with a variable-speed motor enclosed in a temperature-controlled environmental chamber.

Table 2: Commonly used test velocities for Tester 2.

Angular Speed [rpm]	234	280.5	327	374	420	498	560	618	700	796
Equivalent Train Speed [mph]	25	30	35	40	45	53	60	66	70	85

Load was applied to the test bearings via a hydraulic cylinder, seen in Figure 18. The hydraulic cylinder is capable of applying loads that range from 0 to 175% of full load – full load being 34,400 lb_f per bearing as stated in AAR standards for Class F and K bearings, which corresponds to a fully-loaded railcar. The load from the hydraulic cylinder is applied directly to the two centrally located bearings, referred to as "top-loaded" bearings; the reaction load is then evenly distributed to the two outer bearings, referred to as "bottom-loaded" bearings. Because the two centrally located bearings have loading conditions more representative of those seen by bearings in field service, vibration data acquired mainly from those two bearings was utilized for algorithm development.

3.2 Instrumentation Setup

The top-loaded bearings were equipped with Class F or K AdapterPlus™ bearing adapters, complete with an AdapterPlus™ elastomer pad, and were machined to house four accelerometers, two bayonet K-type thermocouples, and an adapter K-type thermocouple. Bottom-loaded bearings rested on all-steel adapters, machined to house two bayonets, and two accelerometers. Accelerometers included an ADI ADXL001-70BEZ (ADXL) mounted on a custom-built circuit board, seen in Figure 19 (left), designed by James Bantz – a fellow graduate student majoring in Electrical Engineering – and a PCB 355B02 (PCB), depicted in Figure 19 (right). One essential difference between the two accelerometers is the filtering system utilized by each. The PCB came equipped with a built-in constant-current signal conditioner [20], while

the ADXL required post-signal filtering, which was accomplished utilizing a sixteenth-order, low-pass filter with a 2.38 kHz cutoff frequency designed and manufactured by James Bantz.

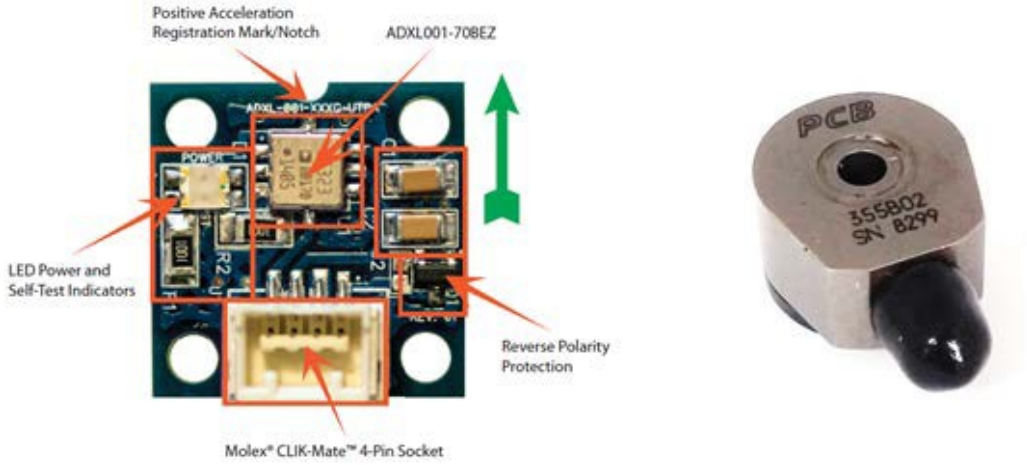

Figure 19: Labeled custom-built ADXL001-70 accelerometer courtesy of James Bantz (left), and PCB 355B02 accelerometer (right).

Thermocouples and accelerometers were mounted on the AdapterPlus™ bearing adapters in the locations indicated in Figure 20. All accelerometers are radially located on the adapter with respect to the bearing. However, to distinguish between the various locations, each position was given its own annotation. Because an ADXL and PCB are secured in a channel unique to a SmartAdapter prototype – a product currently under development by UTPA researchers in conjunction with Amsted Rail – this location was labeled as SmartAdapter (SA) location. Previous research performed at UTPA involved testing of Wireless Sensor Nodes, later referred to as motes by UTPA railroad bearing researchers, developed by IONX, LLC, a subsidiary of Amsted Rail, which were mounted to the lateral surface of the bearing adapter, referred to as the mote (M) location. Since the remaining location does not include any distinguishing characteristics, it is appropriately named the radial (R) location. Bottom-loaded bearing adapter ADXLs and PCBs were secured in the mote and radial locations, respectively. Accelerometers located on B1 and B2 faced inboard (IB, towards pulley), while accelerometers on B3 and B4 faced outboard (OB, away from pulley). Each bayonet was centered on each of the outer ring

(cup) raceways to measure the temperature produced by each. To ensure the accuracy and reliability of the bayonet thermocouples, one K-type thermocouple was affixed to the center of each bearing cup by a hose clamp aligned between the two bayonets. In addition to the thermocouples that monitored the temperatures of the four bearings within the axle assembly, two K-type thermocouples were positioned along either side of the test axle to monitor and record the surrounding ambient temperature. In all, sixteen K-type thermocouples were employed to monitor and record the temperatures of the experimental setup.

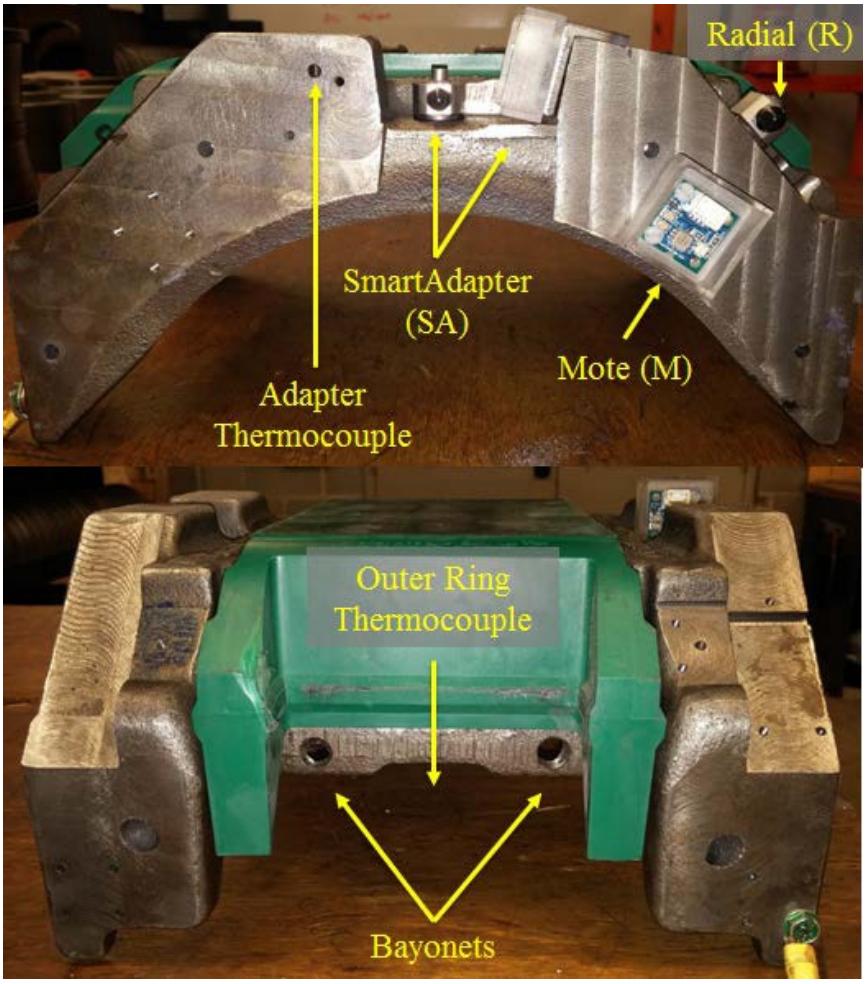

Figure 20: Photograph of indicated accelerometer and thermocouple locations on AdapterPlus™ bearing adapter.

3.3 Data Acquisition

A LabVIEW™ operated National Instruments (NI) cDAQ-9174 data acquisition system (DAQ) was employed to sample and collect data from the sixteen thermocouples and ten accelerometers. The 4-slot chassis was complete with a NI 9213 thermocouple input module, a NI 9215 analog input module, and two NI 9234 analog input modules for the sixteen thermocouples, four ADXLs, and six PCBs, respectively. Temperature data was continuously recorded and sampled every twenty seconds, as opposed to the accelerometer data which was recorded every ten minutes in four-second windows at a sampling frequency of 5.12 kHz. Signal output of the PCB accelerometer was in g's, while the ADXL had an output signal in Volts, which required a post-processing conversion to g's using the accelerometer's sensitivity. This sensitivity was measured by sending a 5V-voltage to the ADXL and recording the accelerometer's output signal, then sending a 0V-voltage and recording its output. Sensitivity was then calculated by subtracting the mean of the low-voltage output from the root-mean-square of the high-voltage output and dividing the resulting voltage by 70 g's. This process was done for each ADXL prior to running the axle assembly. In addition to temperature and vibration monitoring, the power and angular velocity of the variable-speed motor on Tester 2 was recorded utilizing an Omega OMG-CHARTSCAN-1400. Post-processing of all acquired data was performed using MATLAB®.

CHAPTER IV

LABORATORY RESULTS AND DISCUSSION

Demonstration of the effectiveness and accuracy of the optimized Defect Detection Algorithm is provided in this chapter. Laboratory testing of three bearing defect types are analyzed in the following sections. These tests include a bearing containing a (1) cup defect, (2) cone defect, and (3) distributed defect. Unlike the first two test examples, which consist of one top-loaded defective bearing and one top-loaded healthy bearing, the third test includes two top-loaded defective bearings. This test example was conducted in an effort to demonstrate the effect two neighboring defective bearings have on algorithm analysis. All three tests were run on the Chamber Tester under both loading conditions and all ten test speeds, provided in Table 2. Each speed and load combination was operated for at least two hours in order to achieve steady-state conditions.

Analysis was conducted on twelve vibration files recorded for each speed and load iteration. In order to obtain one comprehensive value for each speed and load, the mean of the twelve RMS values and normalized defect energies was calculated for Level 1 and 2, respectively. Mean RMS values of the two top-loaded bearings, Bearing 2 (B2-SA) and Bearing 3 (B3-SA), are compared against the speed-dependent Preliminary and Maximum Threshold RMS values in Level 1 analysis. All Level 1 and 2 results will be summarized in tables for each test example. RMS values greater than the initial threshold in Level 1 tables will be **bolded** and values greater

than the secondary threshold will be ***italicized***. Percentages of the normalized defect energies greater than 50% in Level 2 tables will be **bolded**.

4.1 Laboratory Example: Cup Defect

The first test example includes three healthy bearings and one top-loaded bearing containing a cup defect. The ensuing analysis follows the defect detection algorithm shown in Figure 8.

4.1.1 Level 1: Is the Bearing Defective?

Based on the information provided in Table 3 for Bearing 2, all RMS values are greater than the Preliminary Threshold, indicating this bearing as possibly defective. Of the twenty RMS values, ten are above the Maximum threshold, increasing confidence of defect detection in Bearing 2. At 17% of full load, 80% of RMS values are above the Maximum Threshold. Since Bearing 2 is categorized as defective, the algorithm proceeds on to Level 2.

Table 3 Bearing 2 RMS values at all test speeds and loads in comparison to the Preliminary and Maximum Threshold RMS values.

Speed [rpm]	234	280.5	327	374	420	498	560	618	700	796
Load [%]	17%									
Mean RMS [g]	***1.82***	***2.28***	***2.81***	***3.47***	***3.63***	***4.13***	**4.32**	***5.38***	**6.17**	***9.24***
Load [%]	100%									
Mean RMS [g]	**1.13**	**1.34**	**1.78**	**2.27**	**2.63**	**3.61**	**4.13**	**5.29**	***6.84***	***9.93***
Prelim. Thld. [g]	1.06	1.28	1.51	1.74	1.97	2.35	2.65	2.94	3.34	3.81
Max. Thld. [g]	1.25	1.75	2.25	2.75	3.24	4.08	4.74	5.36	6.24	7.27

Table 4 includes mean RMS values of Bearing 3 at the ten test speeds and two loading conditions which are compared to both thresholds. From the information in Table 4, none of the RMS values are above the Preliminary Threshold, categorizing this bearing as defect-free. Further analysis of Bearing 3 will not be conducted.

Table 4 Bearing 3 RMS values at all test speeds and loads in comparison to the Preliminary and Maximum Threshold RMS values.

Speed [rpm]	234	280.5	327	374	420	498	560	618	700	796
Load [%]	17%									
Mean RMS $[g]$	0.64	0.67	0.83	0.88	1.05	1.18	1.37	1.29	1.50	1.96
Load [%]	100%									
Mean RMS $[g]$	0.45	0.54	0.88	1.07	1.26	1.52	1.70	1.93	1.81	2.16
Prelim. Thld. $[g]$	1.06	1.28	1.51	1.74	1.97	2.35	2.65	2.94	3.34	3.81
Max. Thld. $[g]$	1.25	1.75	2.25	2.75	3.24	4.08	4.74	5.36	6.24	7.27

4.1.2 Level 2: What is the Defect Type?

Due to the results in Level 1 of Bearing 2, Level 2 analysis was required. Following normalized defect energy calculation of the defect frequencies and their harmonics at each of the speeds and loads, the results revealed NDE_{cup} having percentages greater than 50% for all test speeds and loads, indicating a local cup defect present in Bearing 2. The results are summarized in Table 5. Because a local defect is identified, the algorithm will proceed onto Level 3 which estimates the area of the detected defect.

Table 5 Level 2 analysis of Bearing 2 at all test speeds and loads.

Speed [rpm]	234	280.5	327	374	420	498	560	618	700	796
Load [%]	17%									
$\frac{max}{sum} \times 100$ [%]	**52**	**67**	**96**	**81**	**91**	**98**	**99**	**99**	**98**	**62**
Highest NDE	**Cup**	**Cup**	**Cup**	**Cup**	**Cup**	**Cup**	**Cup**	**Cup**	**Cup**	**Cup**
Load [%]	100%									
$\frac{max}{sum} \times 100$ [%]	**82**	**90**	**96**	**94**	**92**	**95**	**93**	**94**	**96**	**95**
Highest NDE	**Cup**	**Cup**	**Cup**	**Cup**	**Cup**	**Cup**	**Cup**	**Cup**	**Cup**	**Cup**

4.1.3 Level 3: What is the Defect Size?

Utilizing the Cup Defect Size Correlation in Figure 15, an estimation of the localized defect's area is calculated. The RMS value at 85 mph and full load (refer to Table 3) is used to calculate the estimated defect area, which is 1.7 $in.^2$. Following teardown and disassembly the Chamber Tester, a thorough inspection of Bearing 2 was conducted. Upon inspection, a spall was discovered on Bearing 2, shown in Figure 21, which had a measured area of 1.9 $in.^2$. The predicted area underestimated the measured area of the cup spall detected in Bearing 2 with a percent error of 12%. The measured area in relation to the Cup Defect Size Correlation is displayed in Figure 22.

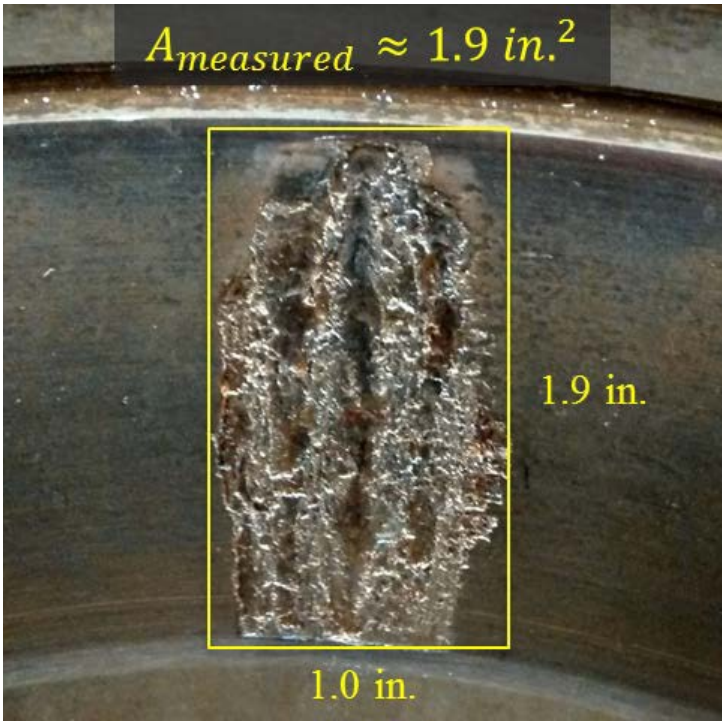

Figure 21 Photograph of the cup spall discovered in Bearing 2 following teardown.

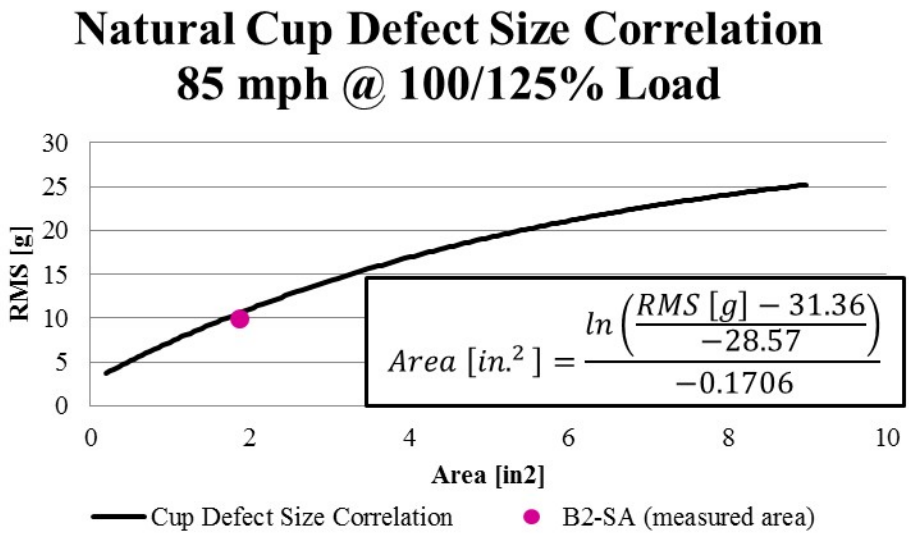

Figure 22 Measured area of Bearing 2 cup spall in relation to Cup Defect Size Correlation.

4.2 Laboratory Experiment: Cone Spall

The second test example consists of three defect-free bearings and one top-loaded bearing containing an inner ring defect. In this example, the phenomenon known as "cross-talk", as mentioned by Alvarado [16], will be introduced.

4.2.1 Level 1: Is the Bearing Defective?

Level 1 analysis presented in Table 6 for Bearing 2, reveals all RMS values are greater than the Preliminary Threshold, categorizing this bearing as possibly defective. Based on this result, the algorithm will proceed onto Level 2.

Table 6 Bearing 2 RMS values at all test speeds and loads in comparison to the Preliminary and Maximum Threshold RMS values.

Speed [rpm]	234	280.5	327	374	420	498	560	618	700	796
Load [%]	17%									
Mean RMS [g]	**1.11**	**1.51**	**1.61**	**2.22**	**2.21**	**2.58**	**2.96**	**3.50**	**3.94**	**4.00**
Load [%]	100%									
Mean RMS [g]	**1.14**	**1.48**	**1.66**	**1.96**	**2.91**	**3.01**	**3.17**	**3.13**	**3.64**	**4.46**
Prelim. Thld. [g]	1.06	1.28	1.51	1.74	1.97	2.35	2.65	2.94	3.34	3.81
Max. Thld. [g]	1.25	1.75	2.25	2.75	3.24	4.08	4.74	5.36	6.24	7.27

The results for Level 1 analysis of Bearing 3 are listed in Table 7. Of the twenty mean RMS values, sixteen are above the Preliminary Threshold, identifying the bearing as defective at these speeds and loads. Level 2 analysis will be performed on the speeds and loads corresponding to bolded RMS values in Table 7.

Table 7 Bearing 3 RMS values at all test speeds and loads in comparison to the Preliminary and Maximum Threshold RMS values.

Speed [rpm]	234	280.5	327	374	420	498	560	618	700	796
Load [%]	17%									
Mean RMS $[g]$	**1.21**	**1.43**	**1.66**	**2.32**	**2.56**	**3.13**	**4.08**	**4.37**	**6.06**	3.50
Load [%]	100%									
Mean RMS $[g]$	0.65	0.87	1.15	**1.80**	**2.14**	**2.90**	**3.79**	**3.38**	**4.17**	**4.92**
Prelim. Thld. $[g]$	1.06	1.28	1.51	1.74	1.97	2.35	2.65	2.94	3.34	3.81
Max. Thld. $[g]$	1.25	1.75	2.25	2.75	3.24	4.08	4.74	5.36	6.24	7.27

4.2.2 Level 2: What is the Defect Type?

After identifying Bearing 2 as defective in Level 1, Level 2 analysis is performed. Normalized defect energy of the defect frequencies and their harmonics at each of the speeds and loads is calculated. The results are shown in Table 8. The results show NDE_{cone} having percentages greater than 50% at 17% of full load for speeds greater than 420 rpm (~45 mph), with the exception of 560 rpm (~60 mph), and full load at speeds greater than 234 rpm (~25 mph), excluding the result at 280.5 rpm (~30 mph). From these results, a localized cone defect is present within Bearing 2. Due to this conclusion, the algorithm will move onto Level 3.

Table 8 Level 2 analysis of Bearing 2 at all test speeds and loads.

Speed [rpm]	234	280.5	327	374	420	498	560	618	700	796
Load [%]	17									
$\frac{max}{sum} \times 100$ [%]	40	34	44	44	**60**	**59**	49	**83**	**59**	**88**
Highest NDE	Cone	Roller	Cone	Roller	**Cone**	**Cone**	Cone	**Cone**	**Cone**	**Cone**
Load [%]	100									
$\frac{max}{sum} \times 100$ [%]	**54**	49	**63**	**71**	**76**	**65**	**54**	**87**	**90**	**94**
Highest NDE	**Cone**	Cone	**Cone**	**Cone**	**Cone**	**Cone**	**Cone**	**Cone**	**Cone**	**Cone**

Because Level 1 detected a possible defect in Bearing 3, Level 2 analysis is conducted. Results of Level 2 analysis in Table 9 reveal NDE_{cone} having percentages greater than 50% at 45 mph in the unloaded and loaded conditions, and 85 mph at full load. The percentage of NDE_{roller} is greater than 50% at 17% of full load at 70 mph. Because four of the RMS values in Table 7 were below the Preliminary Threshold, and only four of the speeds and loads in Table 9 detected localized defects on two different components, Bearing 3 is categorized as a false positive. Note that approximately 19% of defect-free bearings tested in the laboratory are detected as defective when compared to the Preliminary Threshold.

Table 9 Level 2 analysis of Bearing 3 at test speeds and loads in which Level 1 categorized the bearing as defective.

Speed [rpm]	234	280.5	327	374	420	498	560	618	700	796
Load [%]	17									
$\frac{max}{sum} \times 100$ [%]	34	35	37	39	**57**	44	45	41	**55**	
Highest NDE	Cone	Cone	Cone	Roller	**Cone**	Cup	Cone	Cup	**Roller**	
Load [%]	100									
$\frac{max}{sum} \times 100$ [%]				42	**70**	42	43	41	42	**62**
Highest NDE				Cup	**Cone**	Cone	Cone	Cone	Cone	**Cone**

4.2.3 Level 3: What is the Defect Size?

The defect area of the local defect detected in Bearing 2 is estimated using the Cone Defect Size Correlation in Figure 16. The RMS value at 85 mph and full load (refer to Table 6) is inputted into the defect size correlation equation, estimating the defect area as 1 $in.^2$. Following teardown and inspection of Bearing 2, a cone spall was discovered, depicted in Figure 23, which had a measured area of 0.4 $in.^2$. The predicted area overestimated the measured area of the cone spall detected in Bearing 2 with a percent error of 60%. Although this error seems significant, the algorithm still managed to detect a spall that occupies 0.9% of the cone raceway. The measured area in relation to the Cone Defect Size Correlation is exhibited in Figure 22.

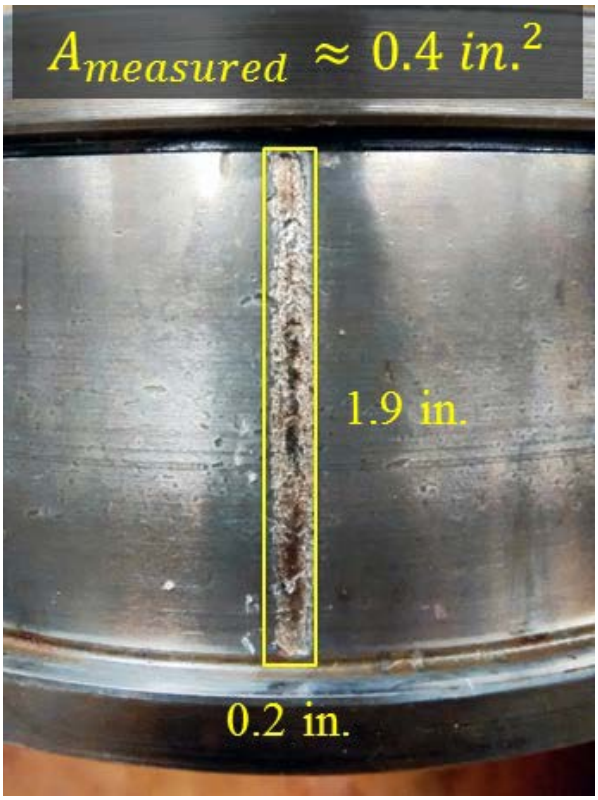

Figure 23 Photograph of cone spall detected in Bearing 2 following inspection.

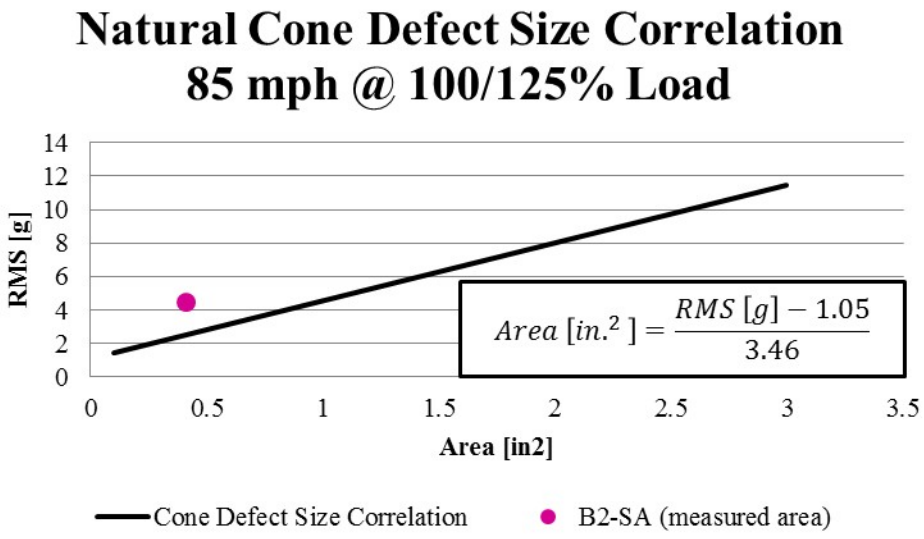

Figure 24 Measured area of Bearing 2 cone spall in relation to Cone Defect Size Correlation.

Inspection of Bearing 3, revealed the absence of a defect. The results in Level 2 can be explained by a phenomenon known as cross-talk – "the ability of a defective bearing to 'share' vibration signatures with the neighboring defect-free bearing" [16]. To demonstrate cross-talk between Bearing 2 and 3, PSDs of each bearing, generated with data collected at 85 mph and full load, are compared in Figure 25. The scaling of the PSD of Bearing 3 was minimized to 0.02 g^2/Hz so that the peaks corresponding to those of Bearing 2 would be distinguished. The red arrows in Figure 25 indicate the instances when ω_{in} harmonics of Bearing 2 are also seen in Bearing 3. The fundamental cone defect frequency of Bearing 2 is indicated for reference.

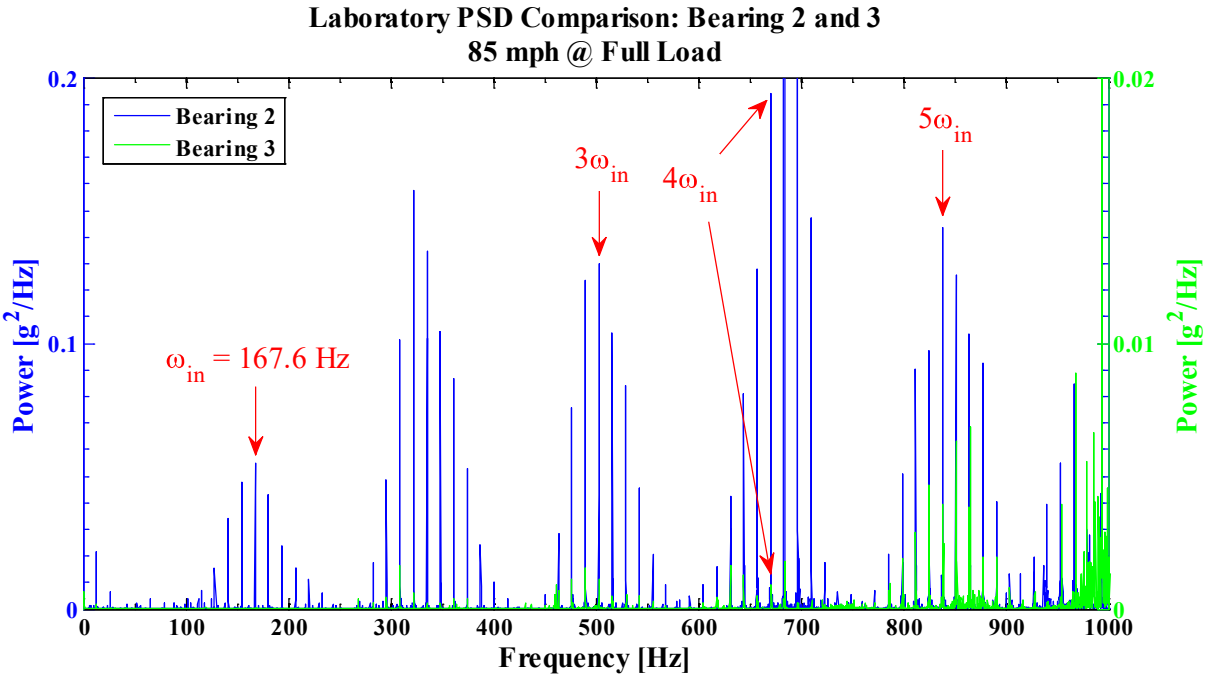

Figure 25 Transposed PSD plots of Bearing 2 and Bearing 3 demonstrating cross-talk at the indicated ω_{in} harmonics.

4.3 Laboratory Experiment: Distributed Defect

The third test example is comprised of two bottom-loaded healthy bearings, one top-loaded bearing with a distributed defect, and one top-loaded bearing containing a cone defect. Demonstration of the ramifications of placing two defective bearings next to one another in a laboratory setting is introduced in this section.

4.3.1 Level 1: Is the Bearing Defective?

Results of Level 1 analysis for Bearing 2 are provided in Table 10. At all test speeds and loads, mean RMS values are above both thresholds, indicating the bearing as possibly defective with increased confidence. Note, 100% of laboratory tested bearing RMS values that fell above the Maximum Threshold were identified as defective.

Table 10 Bearing 2 RMS values at all test speeds and loads in comparison to the Preliminary and Maximum Threshold RMS values.

Speed [rpm]	234	280.5	327	374	420	498	560	618	700	796
Load [%]	17%									
Mean RMS [g]	***1.88***	***2.40***	***3.16***	***4.41***	***6.72***	***6.29***	***8.18***	***7.72***	***11.04***	***11.72***
Load [%]	100%									
Mean RMS [g]	***1.43***	***1.91***	***2.63***	***3.23***	***4.17***	***6.36***	***10.31***	***12.92***	***20.14***	***16.07***
Prelim. Thld. [g]	1.06	1.28	1.51	1.74	1.97	2.35	2.65	2.94	3.34	3.81
Max. Thld. [g]	1.25	1.75	2.25	2.75	3.24	4.08	4.74	5.36	6.24	7.27

Level 1 results of Bearing 3 are presented in Table 11. All twenty mean RMS values are above the Preliminary Threshold, while twelve of the values are above the Maximum Threshold. Based on these results, Bearing 3 is categorized as possibly defective and the algorithm continues onto Level 2.

Table 11 Bearing 3 RMS values at all test speeds and loads in comparison to the Preliminary and Maximum Threshold RMS values.

Speed [rpm]	234	280.5	327	374	420	498	560	618	700	796
Load [%]	17%									
Mean RMS [g]	**1.19**	**1.39**	**1.95**	**2.71**	***3.35***	***5.67***	***5.21***	**4.68**	**4.41**	**5.47**
Load [%]	100%									
Mean RMS [g]	***1.27***	***1.75***	***2.40***	***2.78***	***3.78***	***4.42***	***5.20***	***5.46***	***6.54***	***15.29***
Prelim. Thld. [g]	1.06	1.28	1.51	1.74	1.97	2.35	2.65	2.94	3.34	3.81
Max. Thld. [g]	1.25	1.75	2.25	2.75	3.24	4.08	4.74	5.36	6.24	7.27

4.3.2 Level 2: What is the Defect Type?

Calculation of the normalized defect energies at each of the twenty test iterations discloses fifteen speeds and loads with NDE_{cup} greater than 50%. These speeds and loads include 234 to 618 rpm at 17% of full load, and 234 to 618 rpm at full load, with the exception of 327 rpm. The remaining five speeds and loads indicate local defects on the cone and roller components. These results are supplied in Table 12. In summary, all speed and load iterations have NDEs greater than 50%. Because an individual component did not have an NDE greater the 50%

consecutively for all speeds and loads, the defect detected in Bearing 2 is classified as distributed. Consequently, the algorithm will not proceed to Level 3.

Table 12 Level 2 analysis of Bearing 2 at all test speeds and loads.

Speed [rpm]	234	280.5	327	374	420	498	560	618	700	796
Load [%]	17									
$\frac{max}{sum} \times 100$ [%]	**75**	**52**	**94**	**91**	**94**	**64**	**65**	**84**	**77**	**94**
Highest NDE	**Cup**	**Cup**	**Cup**	**Cup**	**Cup**	**Cup**	**Cup**	**Cup**	**Roller**	**Cone**
Load [%]	100									
$\frac{max}{sum} \times 100$ [%]	**58**	**69**	**59**	**69**	**80**	**74**	**85**	**98**	**89**	**83**
Highest NDE	**Cup**	**Cup**	**Cone**	**Cup**	**Cup**	**Cup**	**Cup**	**Cup**	**Roller**	**Cone**

The results of Level 2 analysis for Bearing 3 are summarized in Table 13. At 17% of full load, three speeds show NDE_{cone} to be above 50%, and two speeds indicate NDE_{cup} with a percentage of 50% or greater. As for the results at full load, two speeds reveal NDE_{cone} greater than 50% while another two demonstrate NDE_{cup} having percentages greater than 50%. Based on the information provided in Table 13, the defect classification remains inconclusive.

Table 13 Level 2 analysis of Bearing 2 at all test speeds and loads.

Speed [rpm]	234	280.5	327	374	420	498	560	618	700	796
Load [%]	17									
$\frac{max}{sum} \times 100$ [%]	36	**65**	40	44	**50**	**55**	48	**60**	**72**	47
Highest NDE	Roller	**Cup**	Cup	Cup	**Cup**	**Cone**	Cup	**Cone**	**Cone**	Roller
Load [%]	100									
$\frac{max}{sum} \times 100$ [%]	39	41	48	**51**	47	45	**78**	**63**	46	**84**
Highest NDE	Cup	Cup	Cup	**Cone**	Cup	Cone	**Cup**	**Cup**	Cone	**Cone**

4.3.3 Level 3: What is the Defect Size?

Upon teardown and disassembly of Bearing 2, inspection revealed defects present on the inner and outer rings, shown in Figure 26. Pitting was observed in the loaded region of the cup spall and across the surface of the cone raceway. The combined defect area of both asperities was measured as 3.5 in.^{2}.

Figure 26 Photographs of the cup (top) and cone (bottom) defects discovered in Bearing 2 following inspection.

Inspection of Bearing 3 unveiled a cone spall, which is seen in Figure 27. Measurement of the area was 0.2 in.^{2}. Difficulty in identifying the defect type may have been a consequence of the defect's small size and cross-talk from the neighboring bearing. Validation of cross-talk is provided in Figure 28, where the arrows indicate instances of cup defect harmonics witness by Bearing 3 from the adjacent top-loaded bearing.

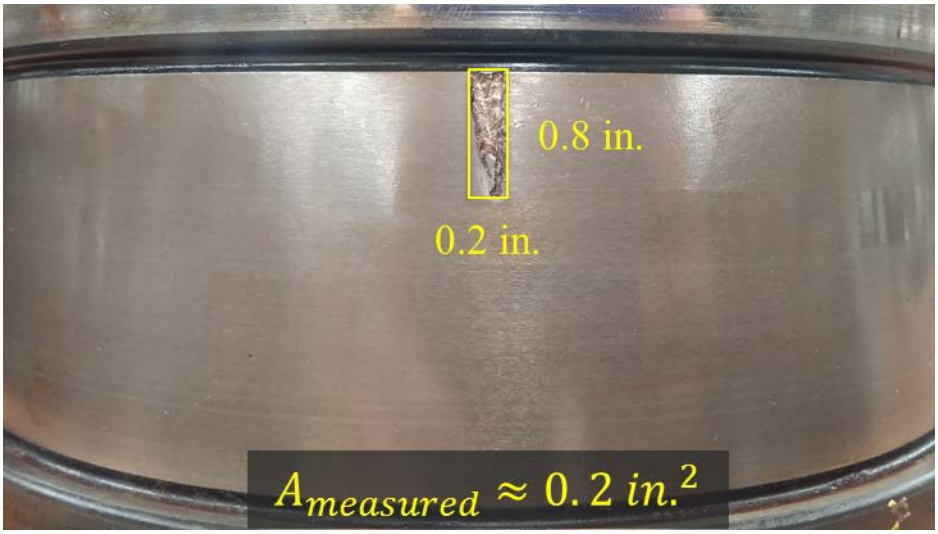

Figure 27 Photograph of cone defect identified in Bearing 3 following teardown and inspection.

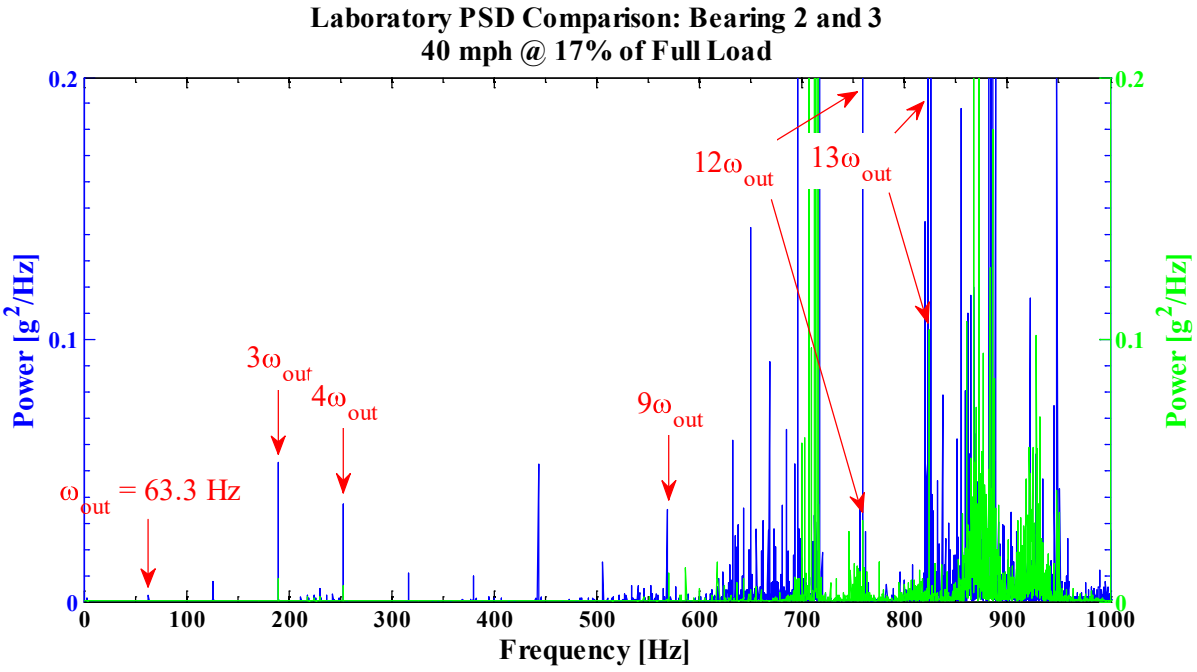

Figure 28 Transposed PSD plots of Bearing 2 and Bearing 3 demonstrating cross-talk at a few of the indicated ω_{out} harmonics.

CHAPTER V

ALGORITHM VALIDATION THROUGH FIELD TESTING

In field service, railroad bearings witness many external vibrations due to track welds, railroad ties, inconsistencies in track geometry, and wheel flats, to name a few. Consequently, some uncertainty may arise from a purely laboratory-developed railroad bearing defect detection algorithm and its ability to detect defective bearings in the field. To address this matter, a proof of concept validation field test was performed at the Transportation Technology Center, Inc. (TTCI) in Pueblo, CO. The test consisted of four defective bearings with poly-cage cone assemblies provided by UTPA and four, presumed, healthy bearings containing steel-cage cone assemblies supplied by TTCI. The railcar on which the bearings were mounted was operated on two test tracks: the Railroad Test Track (RTT) and Precision Test Track (PTT). The RTT is a 13.5-mile loop in which the maximum train operating speed is 165 mph, and the PTT is a 6.2-mile track which is mainly used for tests involving vehicle dynamic behavior, safety compliance, and impact [21]. Following completion of the field test, the four defective bearings were shipped back to UTPA where laboratory testing of the bearings ensued. Analysis of the frequency spectrums from the defective bearings tested in the field revealed the need for minor adjustments in Level 2 of the algorithm. Once these adjustments were incorporated into the defect detection algorithm, the accuracy of Level 2 analysis of the field data acquired from the four defective bearings improved markedly. This chapter summarizes the main results and includes a detailed description of the TTCI field test setup. Adding to the strength of this study, it should be noted

that this field test was a conducted as a blind test; meaning that the person who performed the analysis of the acquired data did not know the number, location, or the type of defect within the bearing (if any). Only select members of the research team who assisted in instrumenting the test railcar and setting up the field test knew this information.

5.1 Test Setup and Procedures

In total, four defective bearings (two containing cup defects and two containing cone defects) were used in the field test. Photographs of the four defective components are provided in Figure 29. The defect area for each of the bearings can be found in Table 14.

Figure 29 Photographs of Bearings L1 cone defect (227623-IB, top left), R2 cup defect (D-01-01397, top right), L3 cup defect (C-10-23446, bottom left), and R4 cone defect (MT-32, bottom right).

Each defect was placed inboard (IB) so that the defect was nearest the wheel and oriented away from the accelerometers. This setup represents a worst case scenario in terms of increased difficulty of defect detection. The locations of each bearing along with their application

direction and corresponding adapters are listed below in Table 14. Bearing position (Column 1) is labeled with a combination of a letter and a number. The letter being an "L" for *left of carriage* or "R" for *right of carriage,* where the orientation of the car is set in the direction of travel, and the number referring to a specific axle. The axles are labeled 1 to 4; Axle 1 being nearest the locomotive and Axle 4 being furthest from the locomotive. A top view depiction of bearing and adapter location can be seen in Figure 30. "Typical" bearing application direction (Column 8) refers to the orientation of the bearing ID relative to the direction of application of the bearing on the axle; meaning, the bearing ID should be read normally from left to right when examining the bearing from the side of the railcar, as exhibited in Figure 31. Note that neither a balance car nor instrumented wheel sets were utilized in this field test.

Table 14 List of bearing locations and other details.

Position	Adapter ID	Bearing Size	Bearing Condition	Defect Size [in.^{2}]	Cup ID	Cone IB	Cone OB	Bearing Application Direction
L1	Adapter 1	K	Cone Defect IB	2.2		227623-IB		Typical
R1	Adapter 2	K	Control					
L2	Adapter 3	K	Control					
R2	Adapter 4	K	Cup Defect IB	5.3	D-01-01397			Typical
L3	Adapter 5	K	Cup Defect IB	1.3	C-10-23446			Typical
R3	Adapter 6	K	Control					
L4	Adapter 7	K	Control					
R4	Adapter 8	K	Cone Defect IB	0.6		MT-32		Typical

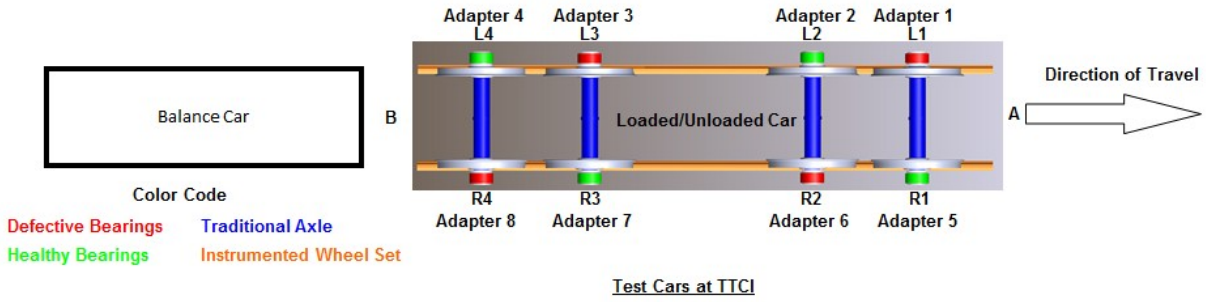

Figure 30 Top view depiction of bearing and adapter locations.

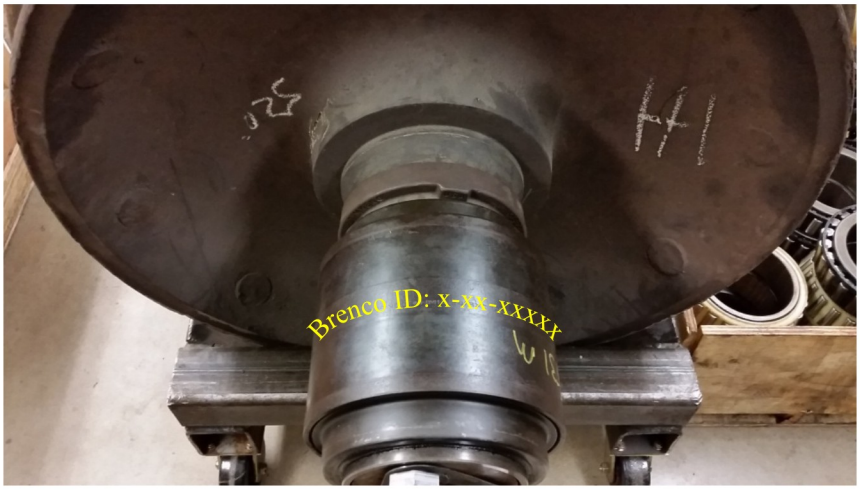

Figure 31 Typical bearing installation.

Sensors were placed outboard (OB) on the bearing adapters. ADI ADXL001-70*g* and PCB 355B02 accelerometers were secured in the SmartAdapter (SA) and Radial (R) location, respectively, as indicated in Figure 32. A K-type thermocouple was secured mid-length of the bearing on the surface of the lower hemisphere with military grade duct tape.

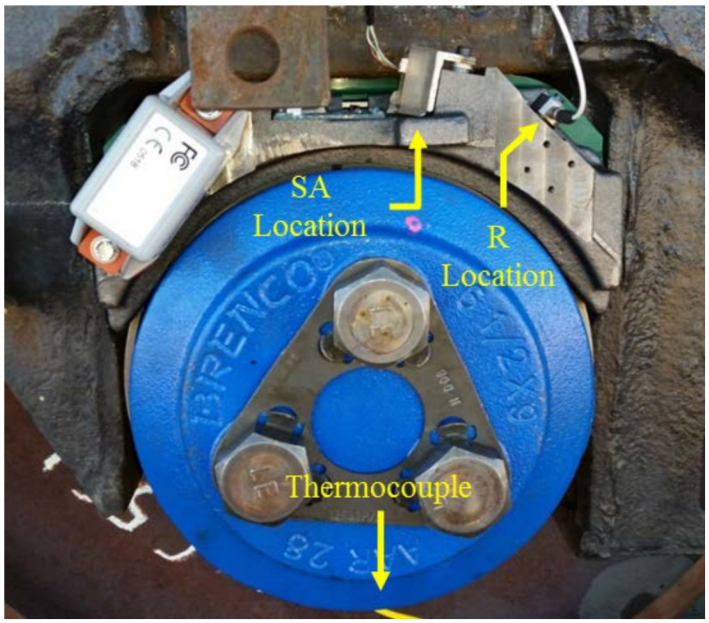

Figure 32 Sensor locations.

The sixteenth order, low pass filter for the ADXLs was fastened to the end of the railcar, as pictured in Figure 33. One constraint of the filter is that it can only support four ADXLs

simultaneously. Due to this limitation, the location of the filter varied between Ends A and B of the railcar, refer to Figure 30, in order to capture the vibration signatures of all eight bearings. Two LabVIEW™ operated National Instruments (NI) data acquisition systems (DAQs) were employed to sample and collect data from the nine thermocouples and sixteen accelerometers. The sampling rates (SR) of the ADXLs and PCBs were 5.556 kHz and 25.6 kHz, respectively. Thermocouple data was averaged and sampled every 15 seconds. Data was recorded continuously to ensure all pertinent testing conditions were captured. New data files were created the moment a desired test speed was reached in an effort to better organize the acquired data. In addition to recording acceleration and temperature data, the locomotive's tachometer data was also collected and monitored, which helped determine when steady state speed was achieved.

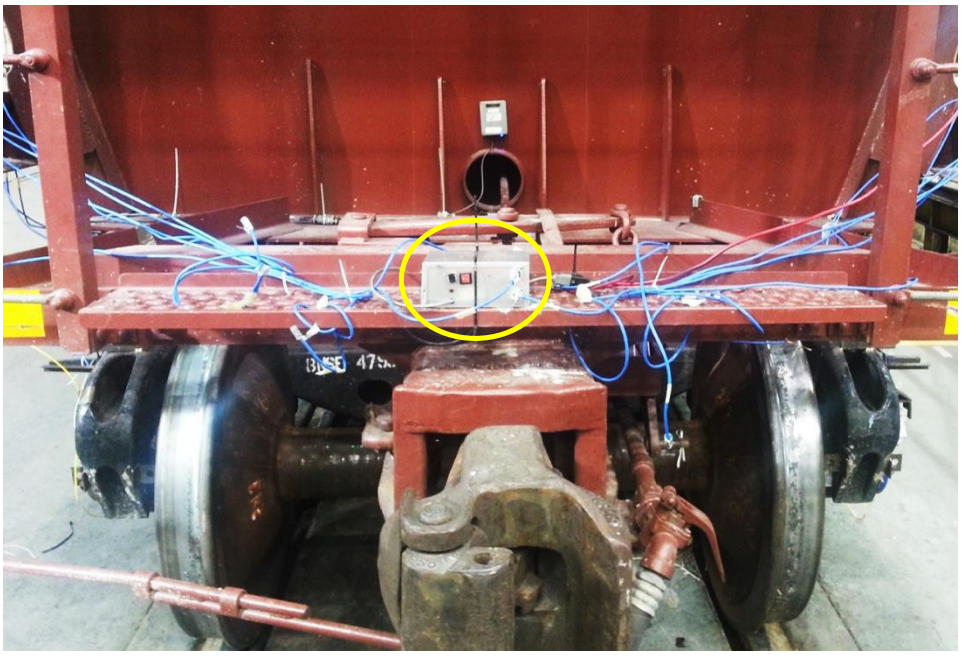

Figure 33 Location of sixteenth order, low pass filter for ADXL accelerometers.

4.2 Field Test Details

5.2.1 Day 1 Testing

Initial testing began on the Railroad Test Track (RTT) with the test car operating at full load. Test speeds included 30 mph, 40 mph, 50 mph, 55 mph, 57 mph and 60 mph. ADXL data was recorded for End A at 30 mph, 50 mph and 55 mph, and End B at 30 mph, 40 mph, 50 mph, 55 mph, 57 mph and 60 mph. On average, iterations lasted approximately two minutes each. As the velocity increased, the testing time decreased due to track length. Because large data files were recorded and collected (files greater than 10 MB), various sample windows within each file were defined for better data analysis. A summary of the number of sample windows analyzed for Day 1 is presented in Table 15. Each sample window (SW) contains four seconds of data. The number of data points within each sample, the sample length, is calculated by multiplying the sampling rate (5.556 kHz for the ADXL data) by the number of seconds per sample (in this case, four seconds). Therefore, each power spectral density curve analyzed in Level 2 of the algorithm is fundamentally generated using 22,224 data points.

Table 15 Number of SWs analyzed for each speed and railcar end during Day 1 on the RTT

Day 1 (100% Load)	***End A***	***End B***
Speed [mph]	**# of SW**	**# of SW**
30	40	40
40	-	40
50	33	34
55	31	31
57	-	29
60	-	27

5.2.2 Day 2 Testing

While the test car remained fully loaded, testing resumed on the Precision Test Track (PTT). The speeds at which testing was conducted included 30 mph, 40 mph, 50 mph and 55 mph.

ADXL data was recorded for both ends of the railcar at all of the aforementioned speeds. Unlike the length of time needed to complete the iterations done on Day 1, the test samples on Day 2 proceeded to almost a quarter of that time as a result of the shorter track length. A summary of the number of sample windows collected for each speed and load is displayed in Table 16.

Table 16 Number of SWs analyzed for each speed and railcar end during Day 2 on the PTT.

Day 2 (100% Load)	***End A***		***End B***	
	Normal Track	**Track Hunting**	**Normal Track**	**Track Hunting**
Speed [mph]	**# of SW Analyzed**	**# of SW Analyzed**	**# of SW Analyzed**	**# of SW Analyzed**
30	45	24	27	
40	33	25	25	33
50	45	33	33	37
55	37	29	29	33

5.2.3 Day 3 Testing

Day 3 testing began on the RTT with an empty (17% of full load) test car. Desired test speeds were 30 mph, 40 mph, 50 mph, 55 mph, 60 mph and 65 mph. ADXL data was recorded for both ends of the railcar at all of the mentioned speeds excluding 30 mph for End A. Each test sample ranged from one and a half minutes to two and a half minutes in duration, depending on the speed of the locomotive. Following the completion of test iterations on the RTT, testing advanced to the PTT where the test speeds included 30 mph, 40 mph and 50 mph. ADXL data was recorded for both ends of the railcar at the previously mentioned speeds excluding 30 mph for End B. Time duration per test iteration ranged from ten seconds to one minute. The number of sample windows collected for each speed and load are summarized in Table 17 and Table 18 for the RTT and PTT, respectively.

Table 17 Number of SWs analyzed for each speed and railcar end during Day 3 on the RTT.

Day 3 (17% Load)	***End A***	***End B***
Speed [mph]	**# of SW Analyzed**	**# of SW Analyzed**
30	-	40
40	39	35
50	32	31
55	55	30
60	20	24

Table 18 Number of SWs analyzed for each speed and railcar end during Day 3 on the PTT.

Day 3 (17% Load)	***End A***		***End B***	
	Normal Track	**Track Hunting**	**Normal Track**	**Track Hunting**
Speed [mph]	**# of SW Analyzed**	**# of SW Analyzed**	**# of SW Analyzed**	**# of SW Analyzed**
30	21	27	-	-
40	37	5	17	5
50	21	5	17	5

For simplicity, the total number of sample windows analyzed for each speed and load throughout the three days of testing at TTCI is summarized in Table 19.

Table 19 Summary of the total number of SWs analyzed for each speed and load throughout the three days of testing.

Day 1 & 2 (100% of Full Load)			***Day 3 (17% of Full Load)***		
Speed [mph]	**End A**	**End B**	**Speed [mph]**	**End A**	**End B**
30	109	67	**30**	48	40
40	58	98	**40**	81	57
50	111	102	**50**	58	53
55	97	93	**55**	29	30
57	-	29	**60**	20	24
60	-	27	**65**	18	25

5.3 Test Results

Initial analysis of the acquired data revealed high variations in RMS values at the beginning and end of various test segments run exclusively on the RTT, as depicted in Figure 34. This event was observed in End A at 17% of full load for speeds of 40, 50, 55, 60, and 65 mph, and End B at 17% of full load for tests run at 55 and 65 mph, and full load at 55 and 60 mph. Cause of these variations in vibration may be due to track related inconsistencies. The region where RMS values were representative of the majority of RMS values recorded, referred to as the "steady state" region, were analyzed in addition to the values recorded on the PTT. An example of the "steady state" region is displayed in Figure 34 bordered by two parallel red lines. An updated summary of the sample windows analyzed is provided in Table 20.

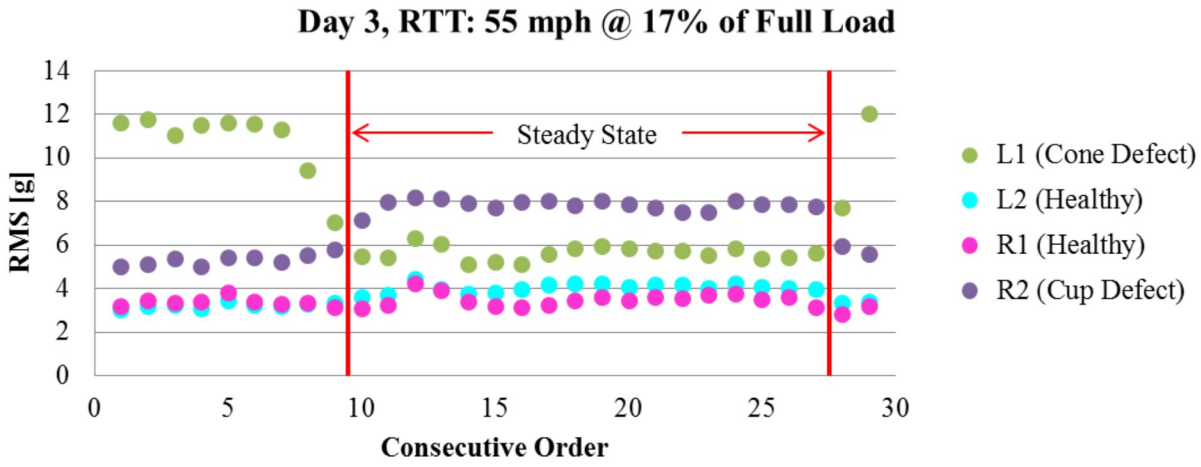

Figure 34 RMS values of the bearings located on End A of the railcar while operating at 55 mph under 17% of full load (unloaded or empty railcar) on the RTT plotted in consecutive order.

Table 20 Updated summary of the total number of SWs that rendered steady state vibration values for each speed and load.

Day 1 & 2 (100% Load)			*Day 3 (17% Load)*		
Speed [mph]	**End A**	**End B**	**Speed [mph]**	**End A**	**End B**
30	109	67	**30**	48	40
40	58	98	**40**	68	57
50	111	102	**50**	44	53
55	97	93	**55**	18	20
57	-	29	**60**	13	24
60	-	19	**65**	12	12

5.3.1 Level 1: Is the Bearing Defective?

More than 90% of RMS values from the sample windows analyzed in Table 20 exceeded the Preliminary Threshold indicating each bearing as possibly defective. In comparison to the Maximum Threshold, more than 80% of RMS values for three of the four test bearings at each speed and load fell above the secondary threshold with the exception being Bearing R4. However, note that R4 is also the bearing with the smallest defect area (refer to Table 14). Recall that the secondary threshold is set in place to error on the side of caution and minimize detection of false positives. The percentages of sample windows with RMS values above the Maximum Threshold for each speed and load are compiled in Table 21 (data collected at full load) and Table 22 (data acquired at 17% of full load). Of the four defective bearings, R4 had the lowest percentages for all speeds and loads.

Table 21 Percentages of SWs with RMS values greater than the Maximum Threshold at full load.

100 % Load	*End A*		*End B*	
Speed [mph]	**L1 (Cone Defect)**	**R2 (Cup Defect)**	**L3 (Cup Defect)**	**R4 (Cone Defect)**
40	100%	83%	92%	59%
50	100%	100%	100%	47%
55	100%	100%	100%	46%
57	-	-	100%	0%
60	-	-	100%	0%

Table 22 Percentages of SWs with RMS values greater than the Maximum Threshold at 17% of full load.

17% Load	*End A*		*End B*	
Speed [mph]	**L1 (Cone Defect)**	**R2 (Cup Defect)**	**L3 (Cup Defect)**	**R4 (Cone Defect)**
40	97%	100%	100%	58%
50	100%	100%	100%	38%
55	100%	100%	100%	40%
60	100%	100%	100%	33%
65	100%	100%	100%	100%

5.3.2 Level 2: What is the Defect Type?

The Level 2 analysis performed was successful in identifying the defects present in L1, R2 and L3 at full load with a majority of the percentages being greater than 50% as revealed in Table 23. Percentages of sample windows able to identify the defects present in the rear located bearings, however, decreased with increasing speed. Further analysis as to the cause of this unfavorable event revealed shifting of the hunted harmonics greater than the provided hunting range, as displayed in the example presented in Figure 35. The hunting range could be increased to capture these out-of-range frequencies, however, this would only be an accommodation to the problem, and not a solution. The solution would be to employ a balanced car to the free end of

the test car, as displayed in Figure 30, as to mimic the setup of a regular train consist in which all railcars are stabilized. Unfortunately, this field test was unable to include such a car.

Table 23 Percentages of SWs having the corresponding defective component's NDE greater than 50% at full load.

Full Load	*End A*		*End B*	
Speed [mph]	**L1 (Cone Defect)**	**R2 (Cup Defect)**	**L3 (Cup Defect)**	**R4 (Cone Defect)**
40	31%	100%	56%	43%
50	78%	99%	56%	5%
55	67%	98%	44%	6%
57	-	-	3%	0%
60	-	-	13%	6%

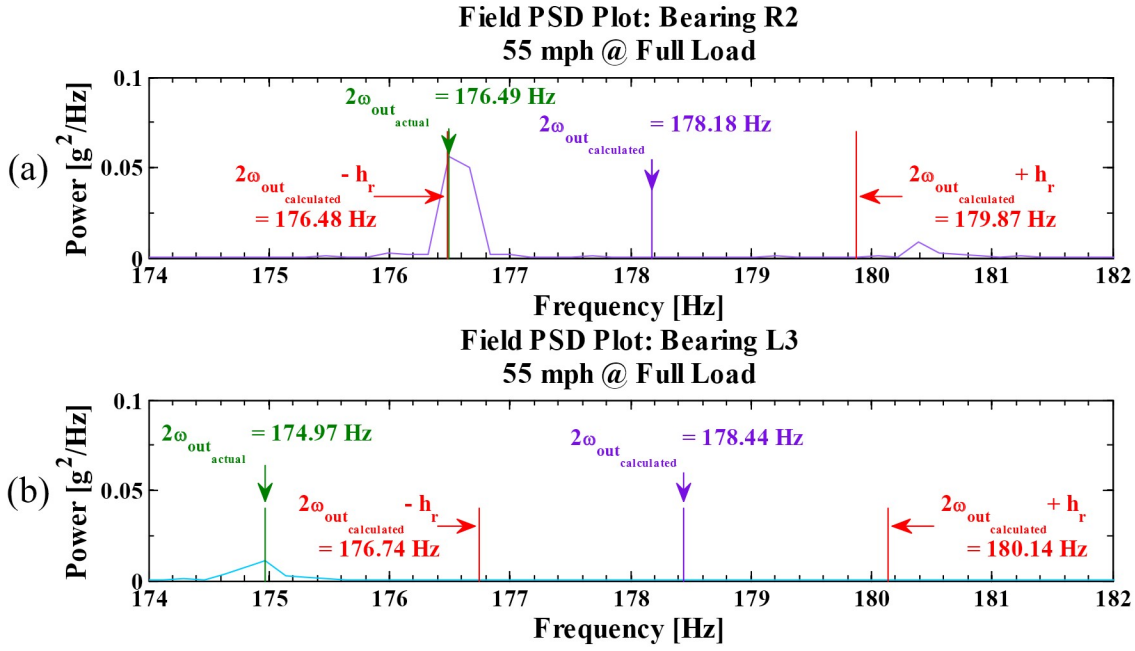

Figure 35 PSD plots of (a) Bearing R2 and (b) Bearing L3 with indicated cup defect frequency locations and hunting ranges.

In general, the defects present at the front end of the railcar were much easier to identify for two main reasons: (1) they were the larger cup and cone defects in terms of spall surface area, and (2) they were not affected as much by the absence of a balance car as was the rear end of the

car. Level 2 analysis of R2 demonstrates great success in identifying the cup defect, as can be seen in the statistics presented in Table 23 and Table 24. The majority of the sample windows for each test speed had NDE_{cup} percentages greater than 50%. The statistics were also good for the cone defect in L1, especially at the high speeds. When comparing the results for Ends A and B in Table 23 and Table 24, one can observe that the percentages seen at the rear end of the railcar are lower than those seen at the front of the railcar for the two reasons mentioned earlier. To further illustrate the effect the absence of a balance car had on bearings located on End B of the test car, a PSD comparison of a bearing in a full load and unloaded condition is exhibited in Figure 36. One can observe from the figure that considerably more vibrations were introduced into the frequency spectrum of a bearing in the unloaded condition due to the lack of a balance car.

Table 24 Percentages of SWs having the corresponding defective component's NDE greater than 50% at 17% of full load.

17% Load	***End A***		***End B***	
Speed [mph]	**L1 (Cone Defect)**	**R2 (Cup Defect)**	**L3 (Cup Defect)**	**R4 (Cone Defect)**
40	3%	47%	0%	42%
50	43%	80%	4%	18%
55	72%	100%	0%	10%
60	100%	100%	8%	0%
65	100%	92%	0%	0%

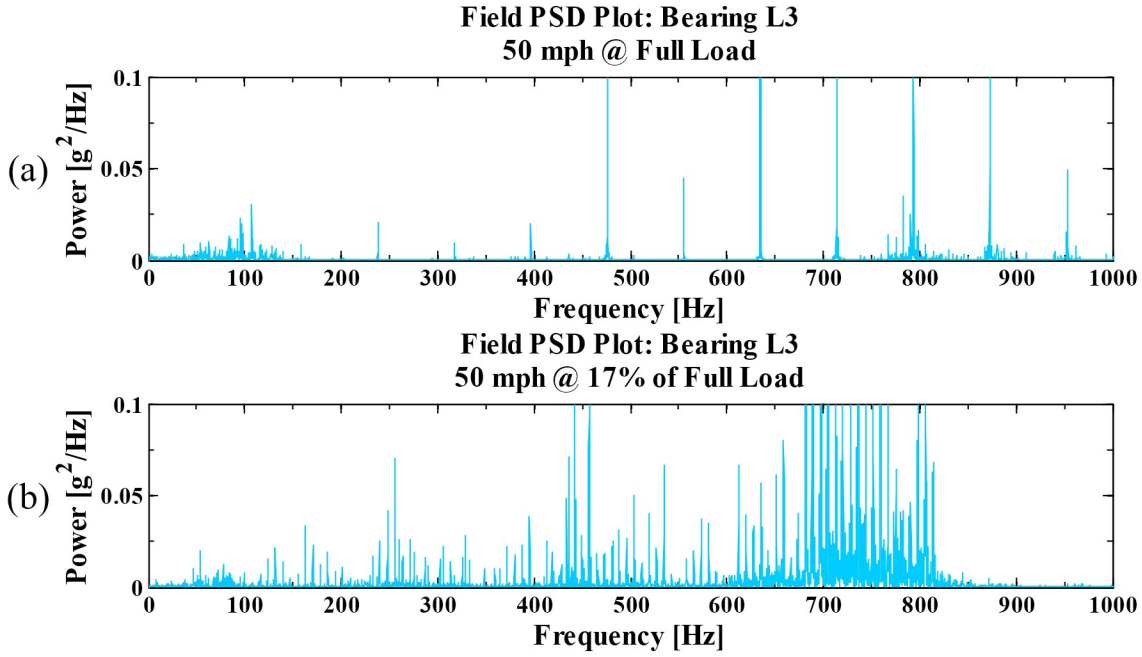

Figure 36 PSD plots of Bearing L3 operating at 50 mph under (a) full load and (b) 17% of full load.

5.3.3 Level 3: What is the Defect Size?

In order to determine which RMS values would be used to estimate the defect areas of the detected defective bearings, Table 23 and Table 24 were analyzed and the speeds and loads with the highest percentages were considered. For Bearings L1 and R2, percentages at 60 and 65 mph at 17% of full load met this criterion. Similarly, this precedent was met for Bearing L3 at 40 and 50 mph, and R4 at 40 mph at full load. To demonstrate that the defect size correlations can accommodate RMS values collected during various speeds and loads, RMS values at four different speeds and both loading conditions were chosen to calculate the estimated defect areas of the four bearings. The selected speeds and loads were 60 mph and 65 mph at 17% of full load, and 50 mph and 40 mph at full load for Bearings L1, R2, L3, and R4, respectively. RMS values from sample windows resulting in NDEs greater than 50% for the corresponding defects in the four test bearings were averaged, producing a single RMS value for each of the elected

speeds and loads. The estimated area and the percentage of the component surface area (A_s) covered by the spalled area for each bearing is provided in Table 25. From the results, the area of the defects within Bearings L3 and R4 were most accurately estimated with less than 10% error. However, when comparing the percentage of surface area covered by the spalled region, the percent error becomes zero. The defect area estimation of Bearing L1 was within 15% error, with the estimated percentage of the cone surface area covered by the defect only off by half a percent from the measured. Of the four bearing defect size estimations, the estimation for Bearing R2 was the outlier, however, based on the data points that make up the defect size correlations in section 2.2.3, outliers will occur, but in minimal quantities. Moreover, as severity of defects increase, the percent error of defect area estimation will decrease as was the case with Bearing R2 which will be discussed in the next section. The locations of the measured areas along with their corresponding averaged RMS values with respect to the defect size correlations are presented in Figure 37 and Figure 38.

Table 25 Measured and estimated defect areas for the defective components within the four defective bearings.

Bearing	***Speed [mph]***	***Load [%]***	***Avg. RMS [g]***	***Estimated Defect Area [in.^{2}]***	***A_s Covered by Estimated Spall Area [%]***	***Measured Defect Area [in.^{2}]***	***A_s Covered by Measured Spall Area [%]***
L1	60	17	8.0	2.0	4.5	2.2	5
R2	65	17	12.2	2.3	4	5.3	10
L3	50	100	8.5	1.3	2.5	1.3	2.5
R4	40	100	3.6	0.7	1.5	0.6	1.5

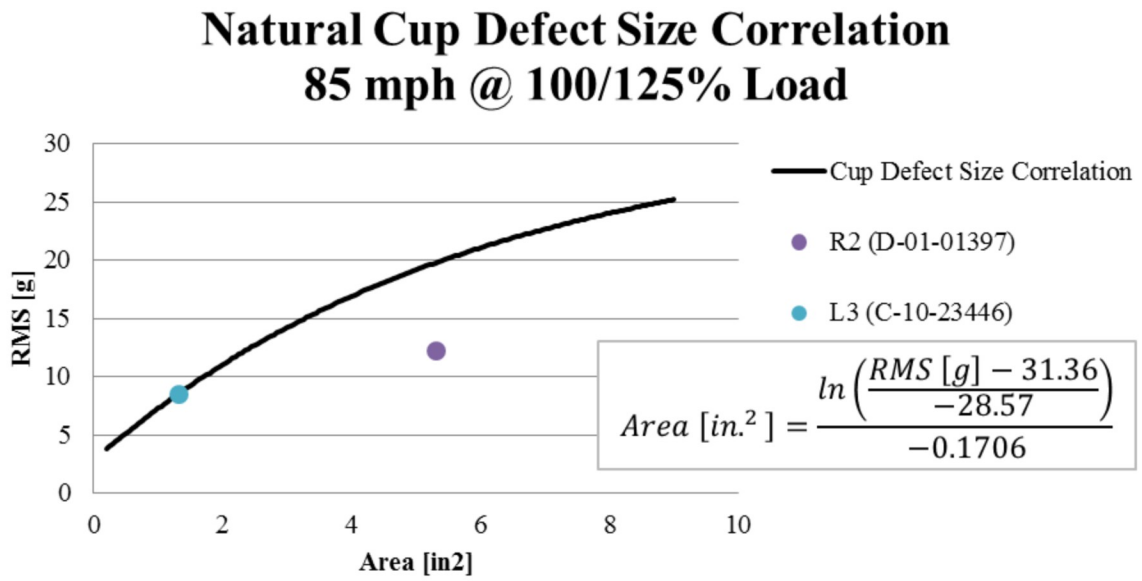

Figure 37 Location of L3 and R2 measured defect areas and their corresponding RMS values on the Cup Defective Size Correlation for 85 mph and 100/125% of full load.

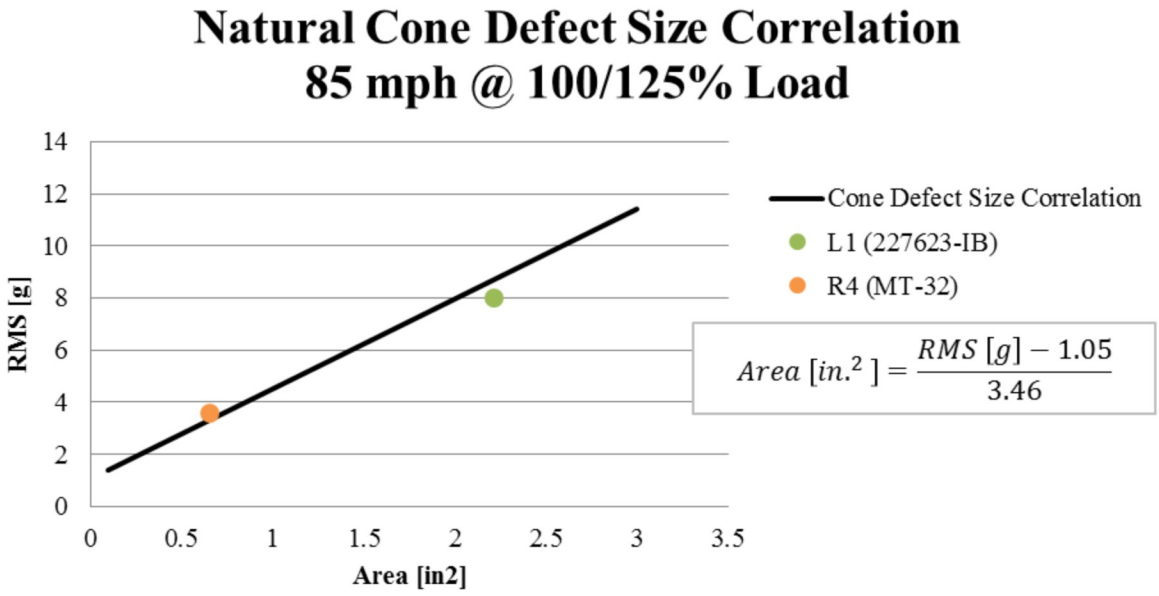

Figure 38 Location of L1 and R4 measured defect areas and their corresponding RMS values on the Cone Defect Size Correlation for 85 mph and 100/125% of full load.

4.4 Laboratory and Field Data Comparison

5.4.1 RMS Comparison

Following the completion of the field test, the four test bearings were shipped back to the University of Texas-Pan American to be re-tested in the laboratory so that the vibration data can be compared to the acquired field data. Prior to laboratory testing, the bearings remained unopened. The only measurements taken before testing were unmounted and mounted lateral. Of the four test bearings, three have been re-tested to date, namely: L1, R2 and R4. The results are plotted in Figure 39 for bearings L1 (top), R2 (middle), and R4 (bottom). The data points in each plot represents an average RMS of an entire data set for a particular speed at a given load, and each series in the figures groups the averaged RMS values recorded at 17% and 100% of full load. RMS values collected in the laboratory are quite comparable to those acquired in the field, excluding L1 for which the laboratory-obtained RMS values are slightly lower than the field RMS values for the corresponding speed. Moreover, all of the laboratory RMS values for the re-tested bearings are above the Average Threshold, which is also true for their corresponding field RMS data, and approximately 30% of the laboratory values are above the Maximum Threshold, as compared to 50% for the field data. The above results are favorable and imply that the thresholds devised from laboratory testing are transferable to field service.

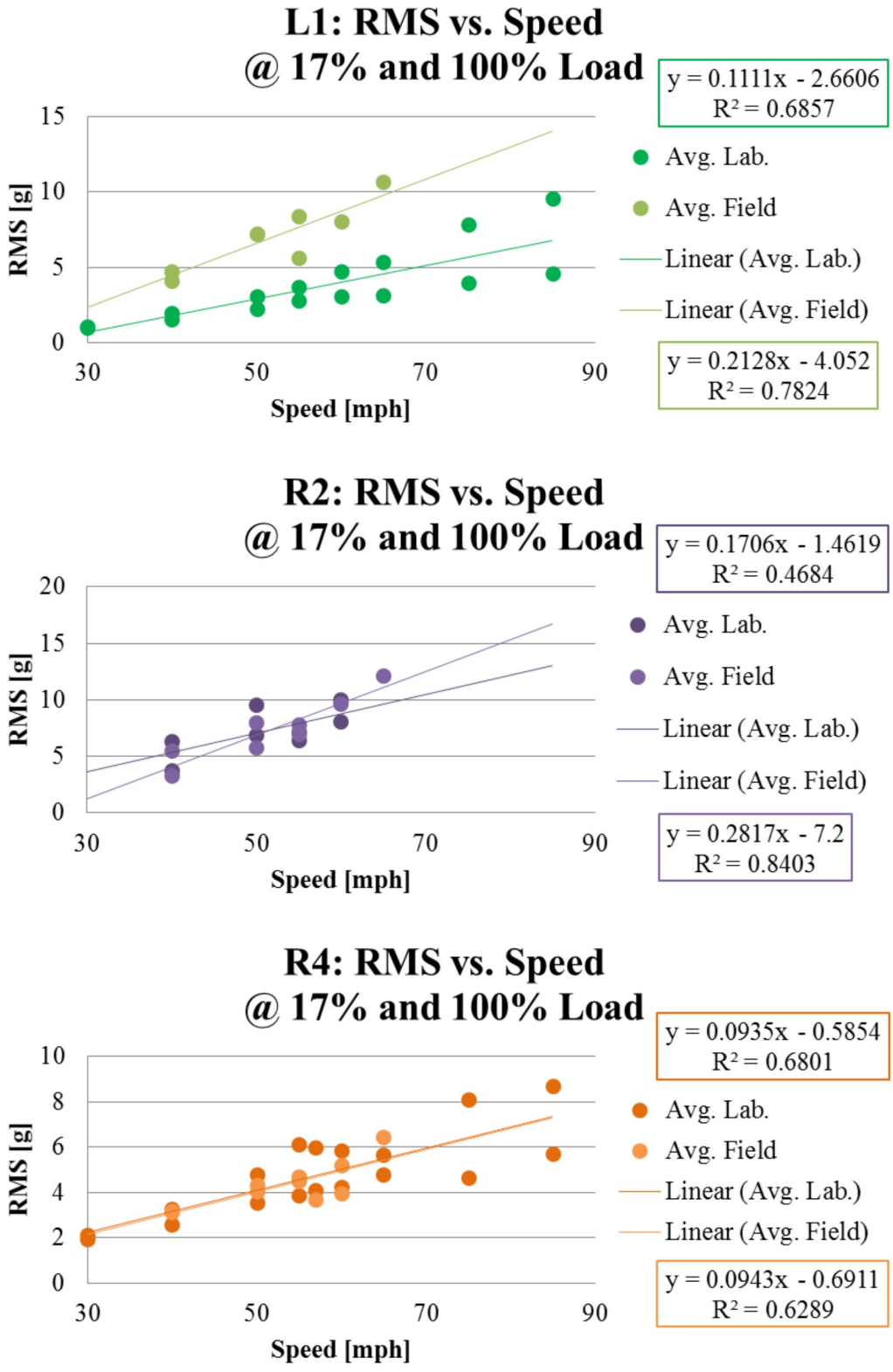

Figure 39 Comparison plots of laboratory- and field-acquired RMS values for Bearings L1 (top), R2 (middle), and R4 (bottom).

Following laboratory testing of Bearing R2, a teardown of the experiment was executed and disassembly and thorough inspection of Bearing R2 ensued. Upon inspection, a considerable deterioration of the detected cup spall was discovered. A comparison of the cup spall prior to field testing and following laboratory testing is exhibited in Figure 40. The spall had grown over 50% of its original size. Figure 41 presents the locations of the defect areas along with their corresponding RMS values prior to and following field and laboratory testing, respectively, with respect to the cup defect size correlation. The defect area estimation of Bearing R2 decreased from over 120% error to less than 15% error following laboratory testing. This event proves that as the severity of a defective bearing increases, the accuracy of area estimation increases.

Figure 40 Photograph of Bearing R2 cup defect prior to field testing (left) and following completion of laboratory testing (right).

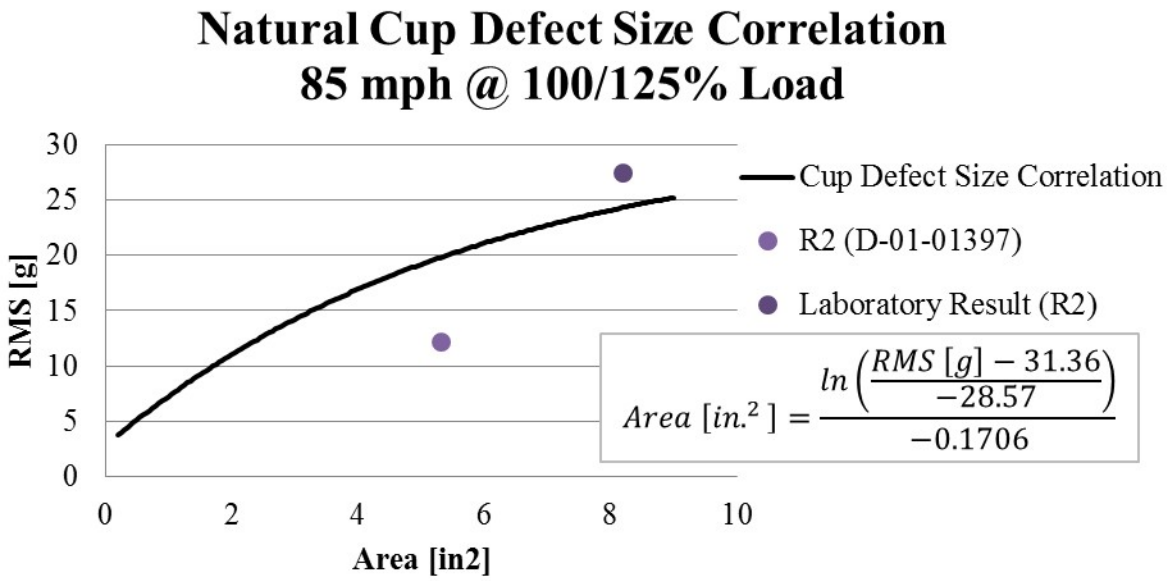

Figure 41 Locations of Bearing R2 cup defect area measurements prior to field testing and following completion of laboratory testing.

5.4.2 PSD Comparison

Initial execution of Level 2 field data analyses was unsuccessful. To determine the underlying problem, an investigation of laboratory versus field PSD plots was performed. The bearing chosen for the in-depth analysis was bearing L1. Data collected at 65 mph and 17% of full load from both the laboratory and field were used to generate the PSDs plotted in Figure 42. When comparing the PSDs side-by-side, one of the first noticeable characteristics is the enhanced noise level between 0 and 150 Hz in the Field PSD Plot, indicated in Figure 42 (b). This particular characteristic causes an issue when hunting for the six fundamental rotational frequencies because the noise levels seem to mask the magnitudes of those six frequencies. To avoid the low-frequency noise present between 0 and 150 Hz, the second level of the algorithm was altered to hunt for harmonics of the fundamental frequencies that fall above this low-frequency region. Therefore, the algorithm was set to hunt for the twentieth, thirty-eighth, fifth, second, second and fifth harmonics of the cone, cage, roller, cup, cone, and roller defect

frequencies, respectively, rather than the fundamental frequencies. This aforementioned modification to the algorithm improved the results for cup defect detection, however, cone defects continued to elude detection.

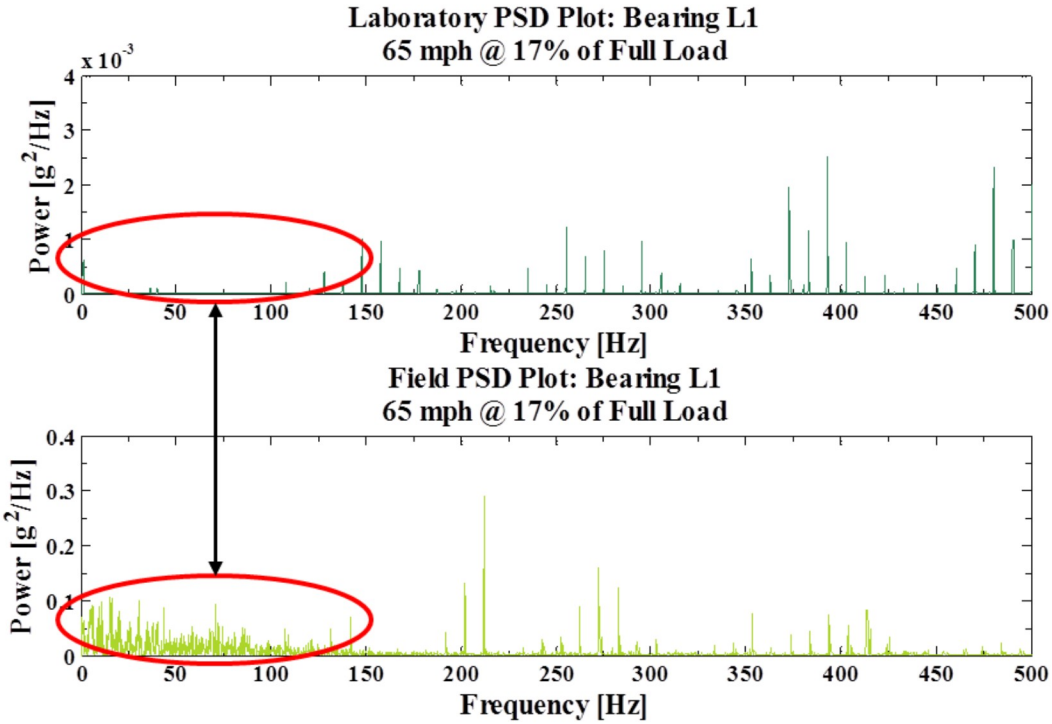

Figure 42 Bearing L1 PSD plot comparison between (a) laboratory-generated data and (b) field-generated data at 65 mph and 17% of full load.

Another distinct feature of the field PSD plot are the prominent peaks, a distance of ω_{cone} apart, present throughout the frequency spectrum. These peaks are similar to those found in a cone defect PSD plot, (reference figure from Chapter 2 containing PSD plots of a healthy bearing, cup, cone, and roller defect) , with the only difference being that the peaks in this PSD do not align with the cone defect ω_{in} harmonics, but instead align with ω_{cone} harmonics, as illustrated in Figure 43. On the contrary, the prominent peaks found in the laboratory PSD plot do not correspond to ω_{cone} harmonics, as can be seen in Figure 44, but rather align nicely with ω_{in} harmonics. The latter behavior is typical of all laboratory-tested cone defects. In order to

understand the abovementioned behavior, the PSD of a presumed healthy field-tested bearing was generated. The healthy bearing chosen for investigation was R1, located on the same axle as L1. The R1 (healthy bearing) PSD, presented in Figure 45, did not exhibit any prominent peaks at ω_{cone} or ω_{in}, which implies that ω_{cone} harmonics present within a frequency-domain plot is characteristic of a bearing with a cone defect in field service. To this end, additional modifications were implemented to Level 2 of the Defect Detection Algorithm to capture ω_{cone} and its harmonics. Rather than utilizing (reference NDE cone equation in Chapter 2) to identify a cone defect in the field, the algorithm now employs Eq. 25, which sums the defect energies for ω_{cone} and ω_{in} frequencies and their harmonics, and normalizes the defect energy by dividing it by the summation of the number of harmonics for each frequency. A similar method is used to identify a roller defect in the field as shown in Eq. 26. These improvements to the algorithm greatly increased the accuracy of defect detection within the field-tested defective bearings.

$$NDE_{cone} = \frac{\sum_{i=1}^{n} \int_{i\omega_{cone}-i_r}^{i\omega_{cone}+i_r} |X(f)|^2 df + \sum_{i=1}^{n} \int_{i\omega_{in}-i_r}^{i\omega_{in}+i_r} |X(f)|^2 df}{n_{cone} + n_{in}} \quad \text{Eq. 25}$$

$$NDE_{roller} = \frac{\sum_{i=1}^{n} \int_{i\omega_{cage}-i_r}^{i\omega_{cage}+i_r} |X(f)|^2 df + \sum_{i=1}^{n} \int_{i\omega_{rolldef}-i_r}^{i\omega_{rolldef}+i_r} |X(f)|^2 df}{n_{cage} + n_{rolldef}} \quad \text{Eq. 26}$$

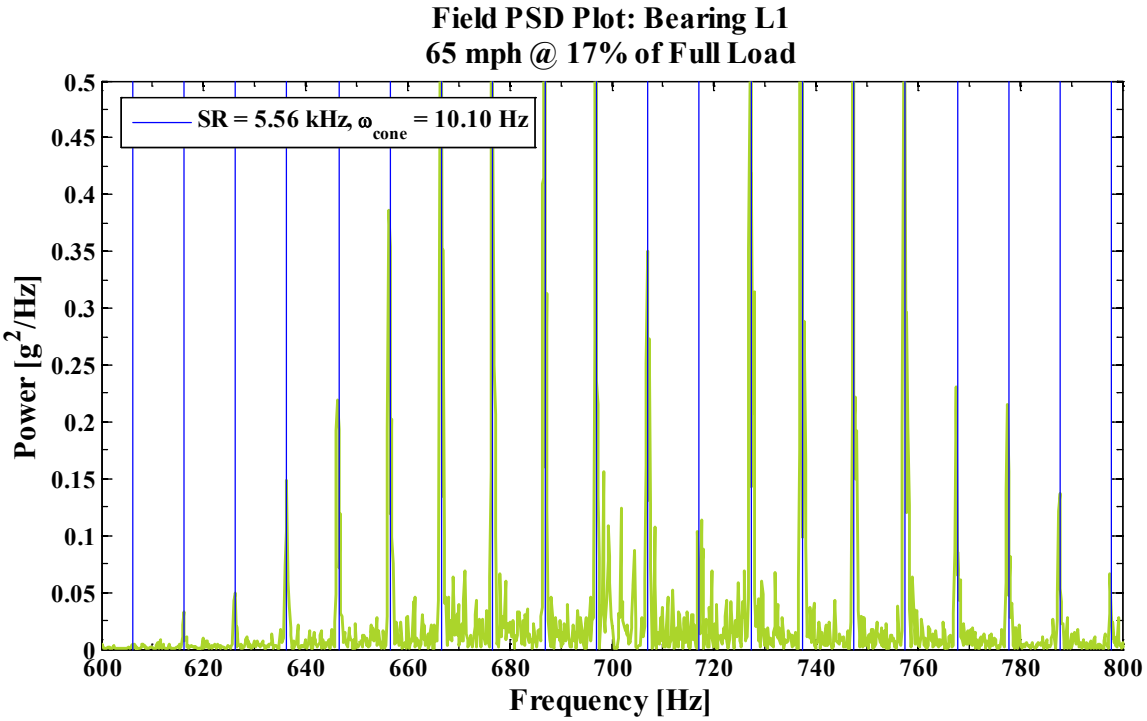

Figure 43 Field PSD plot of L1 at 65 mph and 17% of full load with ω_{cone} defined harmonic lines within 600 and 800 Hz.

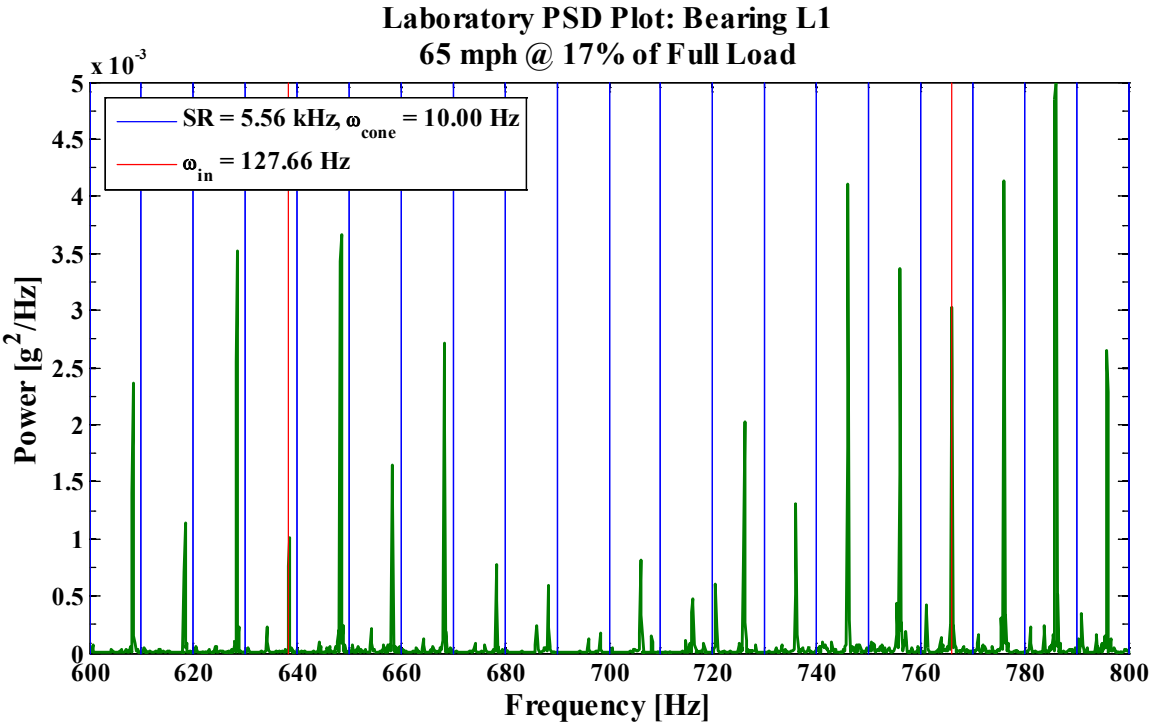

Figure 44 Laboratory PSD plot of L1 at 65 mph and 17% of full load with ω_{cone} and ω_{in} defined harmonic lines within 600 and 800 Hz.

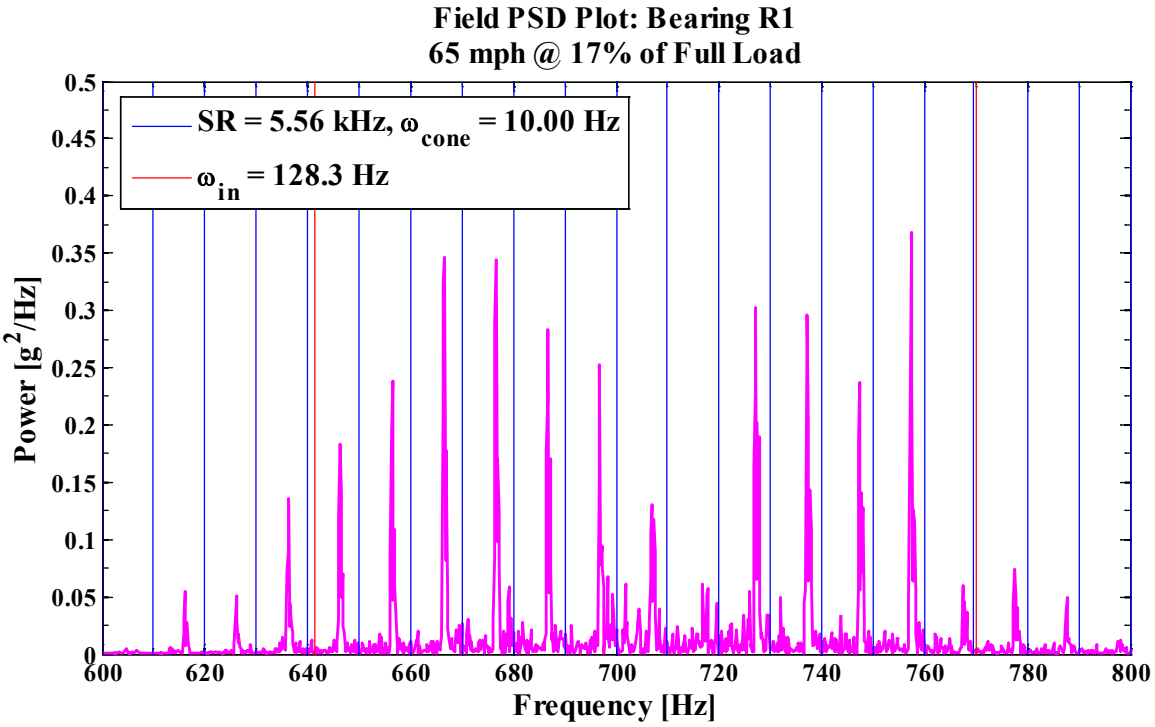

Figure 45 Field PSD plot of R1 (healthy) at 65 mph and 17% of full load with ω_{cone} and ω_{in} defined harmonic lines within 600 and 800 Hz.

CHAPTER VI

CONCLUSIONS AND FUTURE WORK

Notable differences of the developed, optimized, and field-implemented railroad bearing defect detection algorithm from the preliminary algorithm developed by Alvarado [16] include RMS threshold equations, method to determining defect type, and defect area prediction equations. In the initial defect detection algorithm, the first threshold was obtained by correlating average RMS values of defect-free bearings to speed and employing the linear fit equation of that correlation. Similarly, the optimized algorithm utilized the same correlation to establish the initial threshold; however, instead of instituting the linear fit equation as the threshold, better results were observed with the upper bound of the 95% confidence intervals of the mean RMS-to-speed correlation.

Identification of defect type for the preliminary algorithm was achieved by comparing fundamental defect frequency magnitudes to the combined sum of the amplitudes in a method referred to as the Magnitude Criterion. The optimized algorithm utilizes a similar technique, but rather than using the magnitudes, the algorithm utilizes the normalized defect energies of the fundamental defect frequencies and their harmonics. In the field, frequent stoppages of train consists due to the detection of compromised bearing condition can become costly and unnecessary, especially when the detected defective bearings are actually found to be healthy upon disassembly and inspection. For this reason, the Maximum Threshold used to identify distributed defects in the previous algorithm was repurposed to minimize false positives in the

current algorithm. Now, distributed or geometric defects are identified when RMS values are consistently greater than the Maximum Threshold at all speeds and loads, and normalized defect energies of any of the three main bearing components are greater than 50% of the sum of all three normalized defect energies at all operated speeds and loads.

Step three of the preliminary algorithm includes predictions for defect area and perimeter based on speed and RMS utilizing quadratic and linear equations to estimate cup and cone defect areas, respectively, while Level 3 of the current optimized algorithm exclusively estimates area. Similar to the previous algorithm, Level 3 incorporates two equations unique to cup and cone defect areas. However, unlike the quadratic equation used to estimate cup defect size, the Defect Detection Algorithm uses a logarithmic based equation. Additionally, the current defect size correlations are univariate with respect to RMS, and both correlations are comprised of mainly service life test RMS values.

In laboratory tests, the Defect Detection Algorithm was able to accurately detect defective bearings, identify cup, cone, and distributed or geometric defects, and accurately estimate the cup defect area. Additional data is needed to populate the Cone Defect Size Correlation in order to improve the accuracy of cone defect area estimation. RMS values from cup service life tests make up 80% of the Cup Defect Size Correlation. Almost 75% of the cup service life test RMS values were collected from laboratory experiments carried out using the current optimized ADXL noise filter, which provides an ADXL signal comparable to that of a PCB. Since the installation of the new noise filter, no cone service life tests have been conducted. Possible improvement of the Cone Defect Size Correlation can be made by integrating RMS values collected from cone service life tests which will use the current filter. Future work for both

correlations includes developing multivariate defect size correlations in which estimated defect area is a function of speed and RMS.

Analysis from the first laboratory test example accurately detected a localized cup defect present in Bearing 2 which occupied 3.5% of the cup raceway's surface area. Defect area was also estimated with a trivial 12% error. Algorithm analysis of the second test example detected a local defect present on the inner ring of Bearing 2 which had an area covering 0.9% of the cone raceway's surface area. Although the defect area was overestimated with 60% error, the fact that the laboratory-developed Defect Detection Algorithm is able to detect a defect occupying less than 1% of the component's rolling contact surface area is unique and superior to any of the bearing condition monitoring systems currently employed by the rail industry. In addition to identifying local defects, the algorithm was also able to accurately detect a distributed defect contained within Bearing 2. Trackside acoustic detector systems used in the field mainly detect bearings nearing imminent failure, which usually contain distributed defects engulfing more than 20% of a bearing raceways, whereas, the developed algorithm is able to detect a distributed defect with an area that is about 3.5% of the total raceway surface area.

In a field setting, the Defect Detection Algorithm was able to correctly identify all defective bearings in the field. Careful analysis of frequency-domain plots generated from field acquired data revealed that bearings with cone defects exhibited an individual characteristic involving ω_o and its harmonics. Consequently, Level 2 of the algorithm was modified to accommodate this characteristic. With the employed modifications, the performance of Level 2 analysis improved markedly. The Level 2 analysis demonstrated better results for data recorded at full load and bearings located at End A of the railcar, than data recorded for an empty car (17% of full load) and bearings located at End B of the railcar. Implementation of a balance car could have

improved Level 2 performance. Level 3 analysis estimated the defect areas detected and identified in Levels 1 and 2 within a reasonable margin of error as presented in Table 25. After laboratory testing was conducted on the four test bearings from the TTCI field test, RMS values from the field and laboratory were compared. The results revealed that field acquired RMS values are very comparable to those collected in the laboratory, which implies that the thresholds devised from laboratory testing are transferable to field service.

Although the algorithm was successful in identifying the defective bearings in the recent field test, a few measures can be incorporated into the upcoming field test that can significantly improve the outcomes and results. These measures include, (a) employing a balance car in the next TTCI field test to reduce undesired vibrations in the rear end of the railcar, (b) attach load sensors to bearing adapters to determine the exact load applied to each bearing, and (c) test poly-cage defect-free bearings in addition to defective bearings so that the RMS values can be compared to those collected from laboratory tested defect-free bearings.

REFERENCES

[1] AAR-Policy and Economics Department, "Statistics & Publications: Class I Railroad Statistics," 15 July 2014. [Online]. Available: https://www.aar.org/StatisticsAndPublications/Documents/AAR-Stats.pdf. [Accessed 13 October 2014].

[2] CSX Corporation, "CSX Transportation Oil Train Derails at Lynchburg, Va.," [Online]. Available: http://www.csx.com/index.cfm/media/press-releases/csx-transportation-oil-train-derails-at-lynchburg-va/. [Accessed 7 August 2015].

[3] E. Atkin, "For Spilling Crude Oil Into A River, Company Will Pay $361,000," ThinkProgress, 24 February 2015. [Online]. Available: http://thinkprogress.org/climate/2015/02/24/3626212/csx-fined-for-lynchburg-virginia-derailment/. [Accessed 7 August 2015].

[4] M. Martz and R. Springston, "NTSB investigating derailment, oil spill in Lynchburg," Richmond Times-Dispatch, 30 April 2014. [Online]. Available: http://www.richmond.com/news/virginia/article_ca91041c-d096-11e3-ae9b-0017a43b2370.html. [Accessed 7 August 2015].

[5] X. Liu, M. R. Saat and C. P. L. Barkan, "Analysis of Causes of Major Train Derailment and Their Effect on Accident Rates," *Transportation Research Record: Journal of the Transportation Research Board,* no. No. 2289, pp. 154-163, 2012.

[6] Association of American Railroads, "Freight Railroad Capacity and Investment," May 2015. [Online]. Available: https://www.aar.org/BackgroundPapers/Freight%20Railroad%20Capacity%20and%20Investment.pdf. [Accessed 13 August 2015].

[7] D. S. Shah and V. N. Patel, "A Review of Dynamic Modeling and Fault Identifications Methods for Rolling Element Bearing," *Procedia Technology,* no. 14, pp. 447-456, 2014.

[8] Association of American Railroads, "The Impact of the Staggers Rail Act of 1980," May 2015. [Online]. Available: https://www.aar.org/BackgroundPapers/Impact%20of%20the%20Staggers%20Act.pdf. [Accessed 10 August 2015].

[9] Association of American Railroads, "Railroads: Moving America Safely," May 2015. [Online]. Available: https://www.aar.org/BackgroundPapers/Railroads%20Moving%20America%20Safely.pdf. [Accessed 10 August 2015].

[10] Association of American Railroads, "Wayside Detector System," [Online]. Available: http://archive.freightrailworks.org/wp-content/uploads/safety2.pdf. [Accessed 10 August 2015].

[11] Federal Railroad Administration Office of Safety Analysis, "Ten Year Accident/Incident Overview," Federal Railroad Administration, 14 October 2014. [Online]. Available:

http://safetydata.fra.dot.gov/officeofsafety/publicsite/Query/TenYearAccidentIncidentOverview.aspx. [Accessed 14 October 2014].

[12] J. A. Kypuros, C. M. Tarawneh, A. Zagouris, S. Woods, B. M. Wilson and A. Martin, "Implementation of Wireless Temperature Sensors for Continuous Condition Monitoring of Railroad Bearings," in *ASME RTD Fall Technical Conference*, Minneapolis, Minnesota, 2011.

[13] A. Schobel, M. Pisec and J. Karner, "Hot Box Detection Systems as a Part of Automated Train Observation in Austria," *Towards the competitive rail systems in Europe,* pp. 157-161, 31 May 2006.

[14] Transportation Technology Center, Inc., "Vehicle Monitoring Systems," [Online]. Available: https://www.aar.com/pdfs/VehicleMonitoring_OnePager.pdf. [Accessed 7 April 2015].

[15] G. B. Anderson, "Acoustic Detection of Distressed Freight Car Roller Bearings," in *ASME/IEEE Joint Rail Conference & Internal Combustion Engine Spring Technical Conference*, Pueblo, CO, 2007.

[16] I. L. Alvarado, "Defect Detection in Railroad Tapered-Roller Bearings using Vibration Analysis Techniques," University of Texas-Pan American, Edinburg, TX, 2012.

[17] The Mathworks, Inc., "fft," The Mathworks, Inc., 2015. [Online]. Available: http://www.mathworks.com/help/matlab/ref/fft.html. [Accessed 24 July 2015].

[18] C. Tarawneh, J. A. Kypuros, B. Wilson, T. W. Snyder, A. A. Fuentes and B. A. Gonzalez, "A Collaborative On-Track Field Test Conducted to Verify the Laboratory Findings of Bearing Temperature Trending," in *ASME Joint Rail Conference*, Pueblo, CO, 2009.

[19] R. K. Maldonado, "An Investigation into Temperature Trending in Railroad Tapered Roller

Bearings through Vibration Monitoring Techniques," University of Texas-Pan American, Edinburg, TX, 2011.

[20] PCB Piezotronics, Inc., "Model 355B02: Installation and Operating Manual," [Online]. Available: http://www.pcb.com/contentstore/docs/PCB_Corporate/Vibration/Products/Manuals/355B02.pdf. [Accessed 21 July 2015].

[21] Transportation Technology Center, Inc., "Test Tracks," [Online]. Available: http://www.aar.com/tracks.php. [Accessed 11 August 2015].

BIOGRAPHICAL SKETCH

Amy Gonzalez was born in McAllen, Texas, US on January 7, 1991. She attended Weslaco High School and obtained her high school diploma in May 2009. She received her Bachelor of Science from the Mechanical Engineering department at the University of Texas-Pan American in August 2013. During the 2013 Spring semester, Amy was one of two students who received the Academic Deans' Outstanding Students Award for the College of Engineering and Computer Science. In the fall of that same year, she was awarded 3rd place for the HESTEC (Hispanic, Engineering, Science, and Technology) poster presentations, where she presented her research in defect detection of railroad tapered roller bearings. She continued her education at the University of Texas-Pan American and obtained her Master of Science degree in Mechanical Engineering in August 2015. For the 2013-2014 academic school year, Amy received two scholarships: the STEM Success Scholarship, which covered her graduate tuition at UTPA, and the Women's Transportation Seminar-San Antonio Region (WTS-SAR) Graduate Scholarship in the amount of $2,500. In the 2015 Spring semester, she received, once again, a WTS-SAR Graduate Scholarship in the amount of $1,000. During that same semester, she took part in a Field Test at TTCI (Transportation Testing Center, Inc.) in Pueblo, CO where she contributed invaluably to instrumenting the railcars and acquiring data that validated her thesis laboratory findings. Amy Gonzalez currently resides at 2510 North Lane, Weslaco, TX 78599.